The Paleozoic

Nouro, Sardinia

http://www.flickr.com/photos/parossi/451297864/

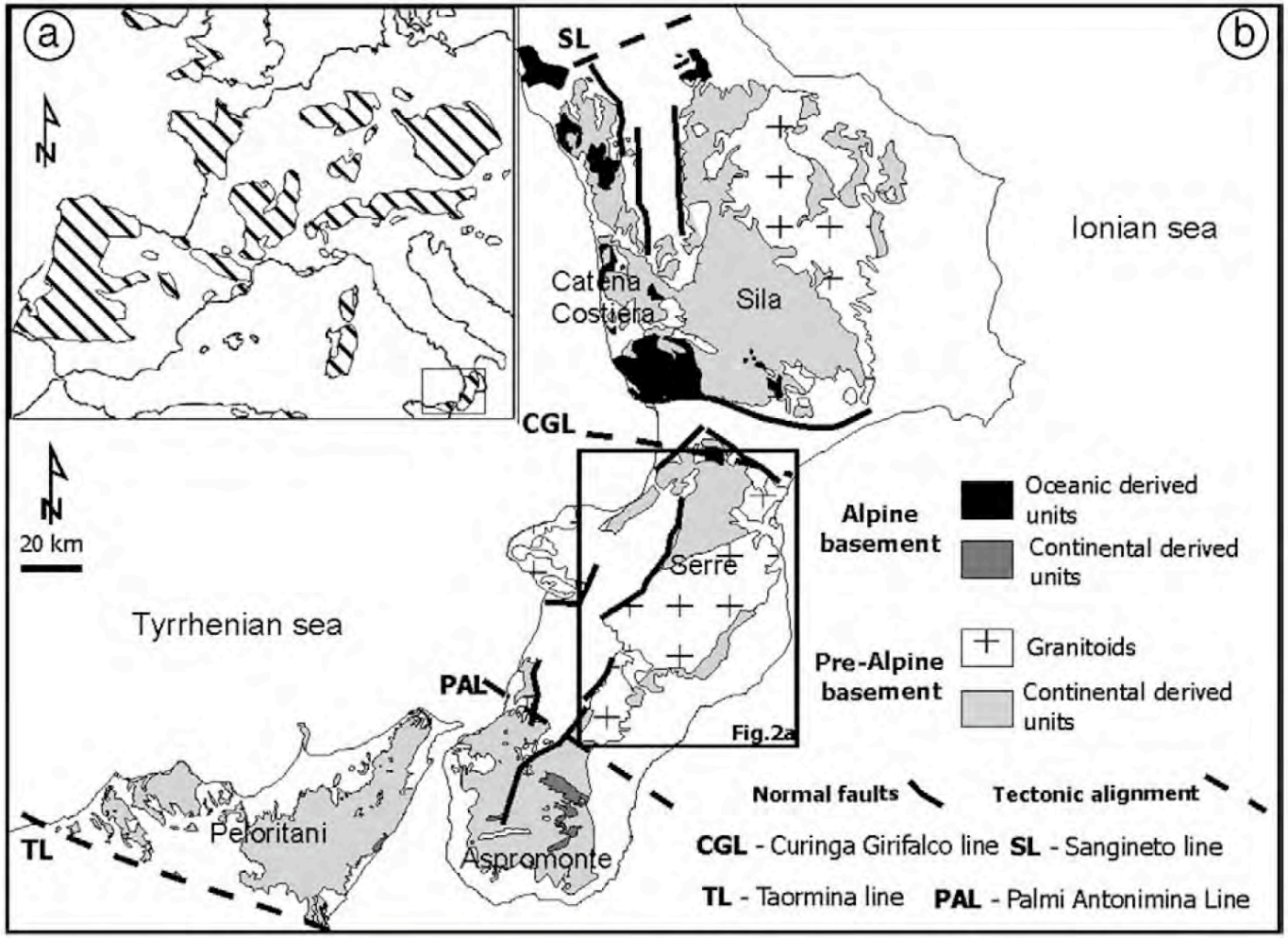

Fig. 1. (a) Distribution of pre-Alpine basement in Europe (after von Raumer et al., 2002). (b) Distribution of Alpine and pre-Alpine (Hercynian and/or pre-Hercynian) basement rocks in Calabria–Peloritani Orogen and main tectonic alignments.
Modified after Atzori and Vezzani (1974), Amodio Morelli et al. (1976), Schenk (1990), Bonardi et al. (2001), Ortolano et al. (2005), Fazio et al. (2008).

Angie et al 2010

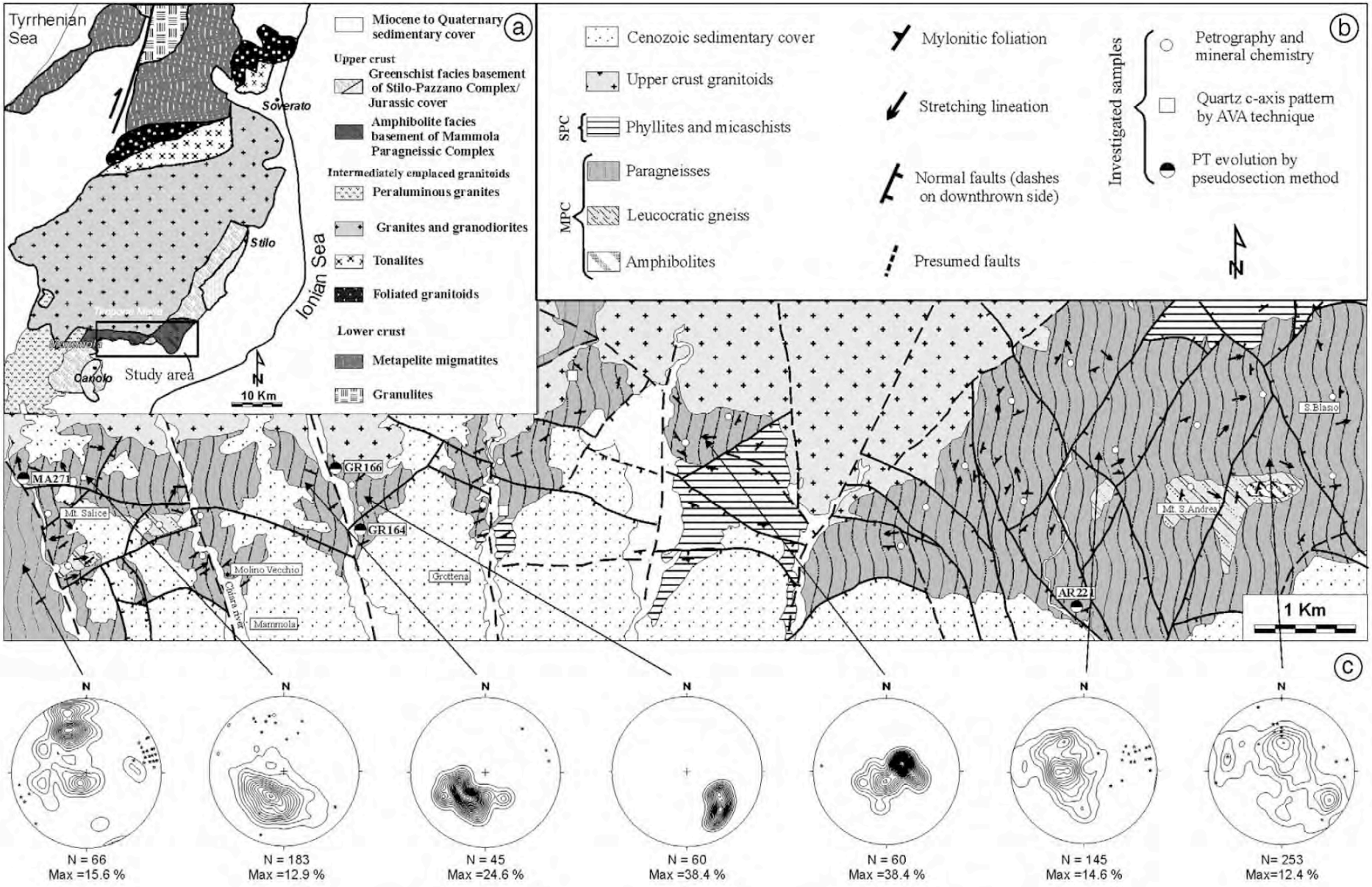

Fig. 2. (a) Geological sketch-map of Serre Massif and location of study area (modified after Graeßner et al., 2000). (b) Geological–structural map of study area and sample locations. (c) Stereoplots (lower hemisphere) with location of structural field stations containing contours of mylonitic foliation S_3 and plunges of stretching lineation.

Angie et al 2010

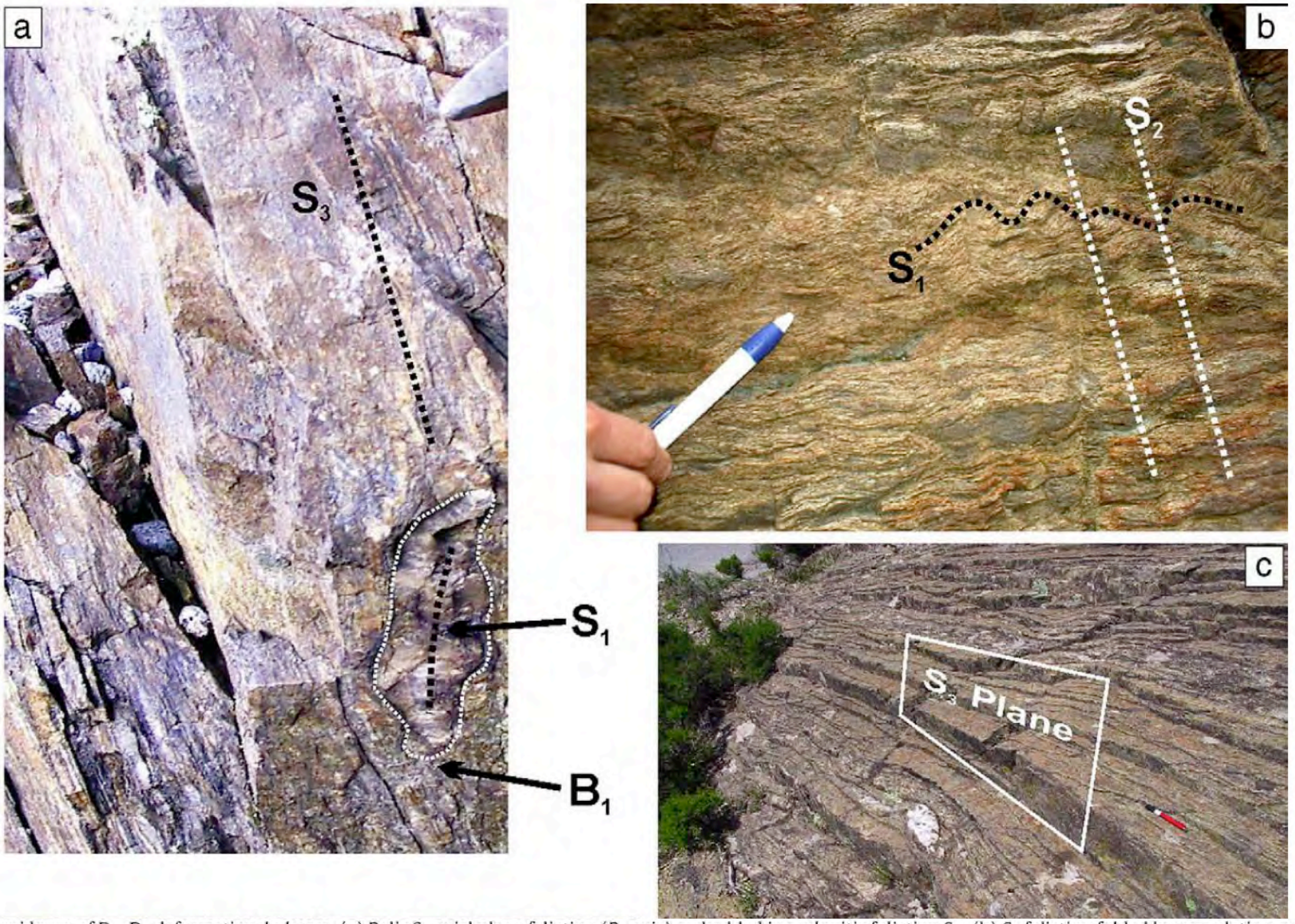

Fig. 3. Field evidence of D_1–D_5 deformational phases. (a) Relic S_1 axial plane foliation (B_1 axis) embedded in mylonitic foliation S_3; (b) S_1 foliation folded by crenulation event (D_2) leading to local formation of S_2 foliation; (c) Example of pervasive sub-vertical mylonitic foliation (S_3); (d) Asymmetric intrafoliar fold in quartz–feldspar level of mylonitic paragneiss; (e) Field relationships between S_3 foliation and late- to post-tectonic magmatic dykes with detail of interfingered boundary between host rock and late-tectonic dyke; (f) Post-tectonic undeformed leucogranite dyke discordantly cutting the mylonitic foliation S_3; (g) Thrust plane produced by brittle deformational stage D_5, resulting from evolution of shallow seated asymmetrical folding of D_4 deformational stage.

Angie et al 2010

Fig. 3. Field evidence of D_1–D_5 deformational phases. (a) Relic S_1 axial plane foliation (B_1 axis) embedded in mylonitic foliation S_3; (b) S_1 foliation folded by crenulation event (D_2) leading to local formation of S_2 foliation; (c) Example of pervasive sub-vertical mylonitic foliation (S_3); (d) Asymmetric intrafoliar fold in quartz–feldspar level of mylonitic paragneiss; (e) Field relationships between S_3 foliation and late- to post-tectonic magmatic dykes with detail of interfingered boundary between host rock and late-tectonic dyke; (f) Post-tectonic undeformed leucogranite dyke discordantly cutting the mylonitic foliation S_3; (g) Thrust plane produced by brittle deformational stage D_5, resulting from evolution of shallow seated asymmetrical folding of D_4 deformational stage.

Angie et al 2010

Relationship between deformational and crystallisation stages in various events of metamorphic evolution.

	Orogenic metamorphic cycle						Thermal metamorphism	
Metamorphic evolution	Prograde evolution			Retrograde evolution			Static events	
Deformational phases	early D_1	late D_1	D_2	D_3			–	
Field evidence	–	Relics of isoclinalic folding surfaces S1 within mylonitic foliation (S3)	Local transposition of S1 surface and formation of a S2 crenulation cleavage	Pervasive mylonitic foliation S3			Randomly oriented biotite plates and cm-size andalusite and cordierite spots	
Metamorphic events	early-M_1	late-M_1	M_2	early M_3	late M_3		M_4	late M_4
Petrographic features	S1 defined by straight to sigmoidal inclusion trails of zoisite in garnet cores	Zoisite-free outer core garnet in equilibrium with biotite, plagioclase, white mica	S2 crenulation schistosity	Biotite, chlorite, white mica, plagioclase intergrowth in garnet rim embayments	Mylonitic foliation S3 given by s- and d-type porphyroclasts wrapped by chlorite, white mica, biotite, feldspar; S/C fabrics; shear bands; oblique foliation		Foaming texture in ribbon-like quartz domains; randomly oriented porphyroblasts; sub-euhedral to euhedral inclusion-free garnet rim	Later retrograde static blastesis of chlorite on previous cordierite blasts and sericitisation of andalusite rims
Crystallisation events	Syn	Syn Post	Syn Post	Syn	Syn			
Quartz	———	———————	———	———————	———		———————————	
White mica	———	– High Phg content –	———	———————	———		———–Low Phg content———	
Biotite	———	———————	———	———————	———		———————————	
Cordierite							———————	
Staurolite							———————	
Chlorite				———	———		———————	
Plagioclase		-Oligoclase-Andesine-		–Albite–	–Oligoclase–		———Oligoclase-Andesine——	
Garnet	———	———————		-High Sps content-			——High Alm–Sps content———	
Clinozoisite	———							
Epidote				———————	———			
Andalusite							———————	
Sillimanite							———	
Tourmaline					———			

Angie et al 2010

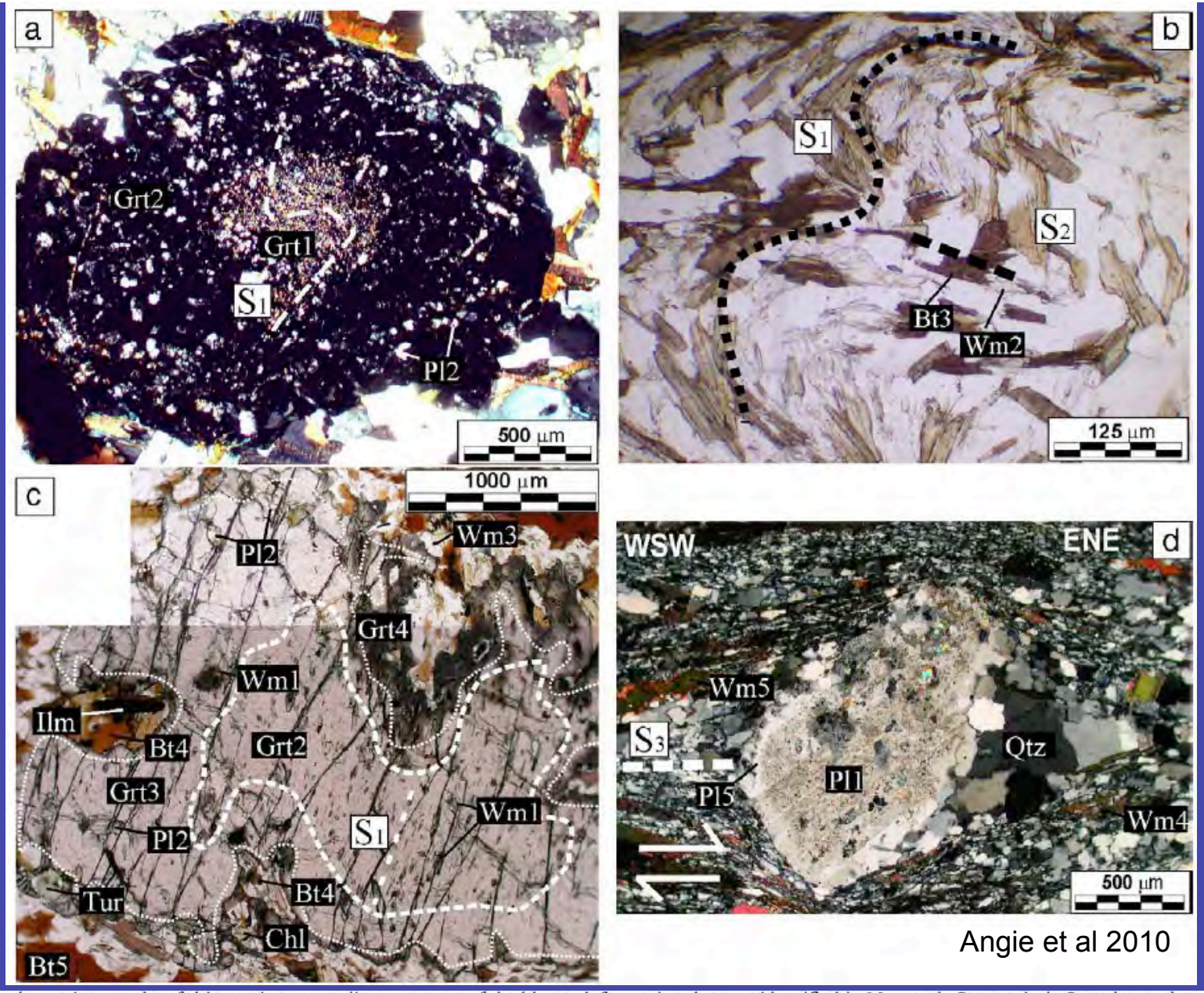

Fig. 4. Representative photomicrographs of thin sections regarding sequence of the blasto-deformational stages identified in Mammola Paragneissic Complex rock types. (a) Early-M_1 assemblage given by tiny zoisite inclusion trails within garnet core (Grt_1) in association with Pl_1, Bt_1, and Qtz and prograde garnet overgrowth (Grt_2) in equilibrium with Pl_2 and $Wmca_1$ (crossed polars); (b) S_2 schistosity defined by blastesis of Qtz + $Wmca_2 \pm Bt_3$ developed during crenulation event D_2 (parallel polars); (c) Prograde to peak assemblages are represented by zoisite-free garnet outer core (Grt_2) in equilibrium with $Wmca_1$ and Bt_2 and by later overgrowths of Grt_3 with Pl_2. Early-M_3 retrograde stage is documented by garnet embayments filled by intergrowths of $Wmca_3 + Pl_3 + Bt_4 + Chl + Ilm$ in equilibrium with garnet rim overgrowth (Grt_4) (parallel polars); (d, e) Non-coaxial syn-mylonitic structures linked to late-M_3 retrograde stage, producing $Wmca_4 + Chl + Ep + Pl_5$ assemblage. σ-type porphyroclast (d) provides a top-to-ENE–NE sense of shear (crossed polars); boudinaged

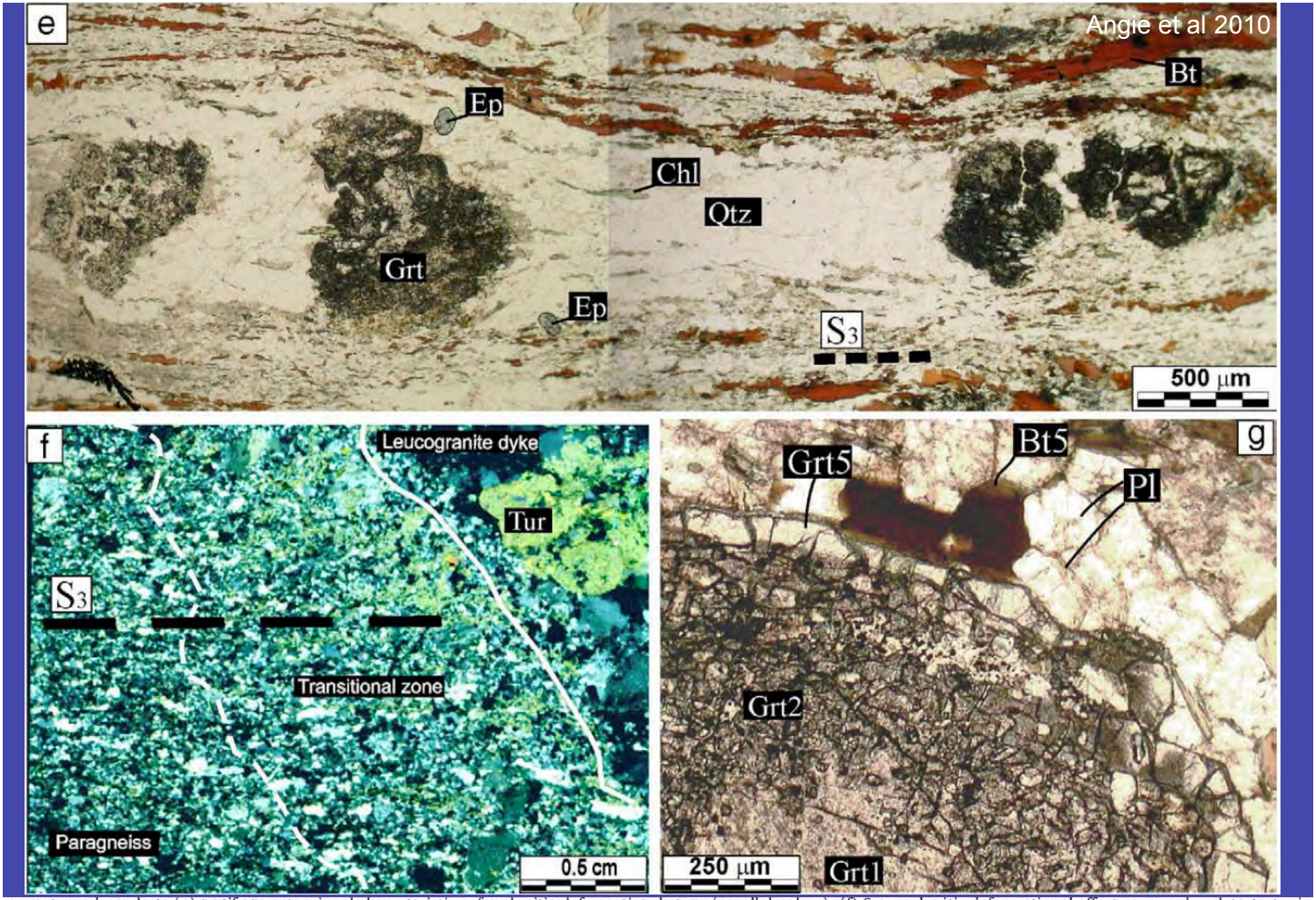

garnet porphyroclasts (e) testify to extensional characteristics of mylonitic deformational stage (parallel polars); (f) Syn-mylonitic deformational effects exposed on late-tectonic leucogranite dyke. Microphotograph shows a transitional zone developed at contact between late-tectonic dyke and mylonitic paragneiss (see Fig. 3f) (high resolution scan: crossed polars); (g) Effects of thermal metamorphism, revealed by static Grt_5 growth forming limpid rims on previous syn-tectonic garnet, in equilibrium with porphyroblastic plagioclase (Pl_5) and biotite (Bt_5) (parallel polars).

Angie et al 2010

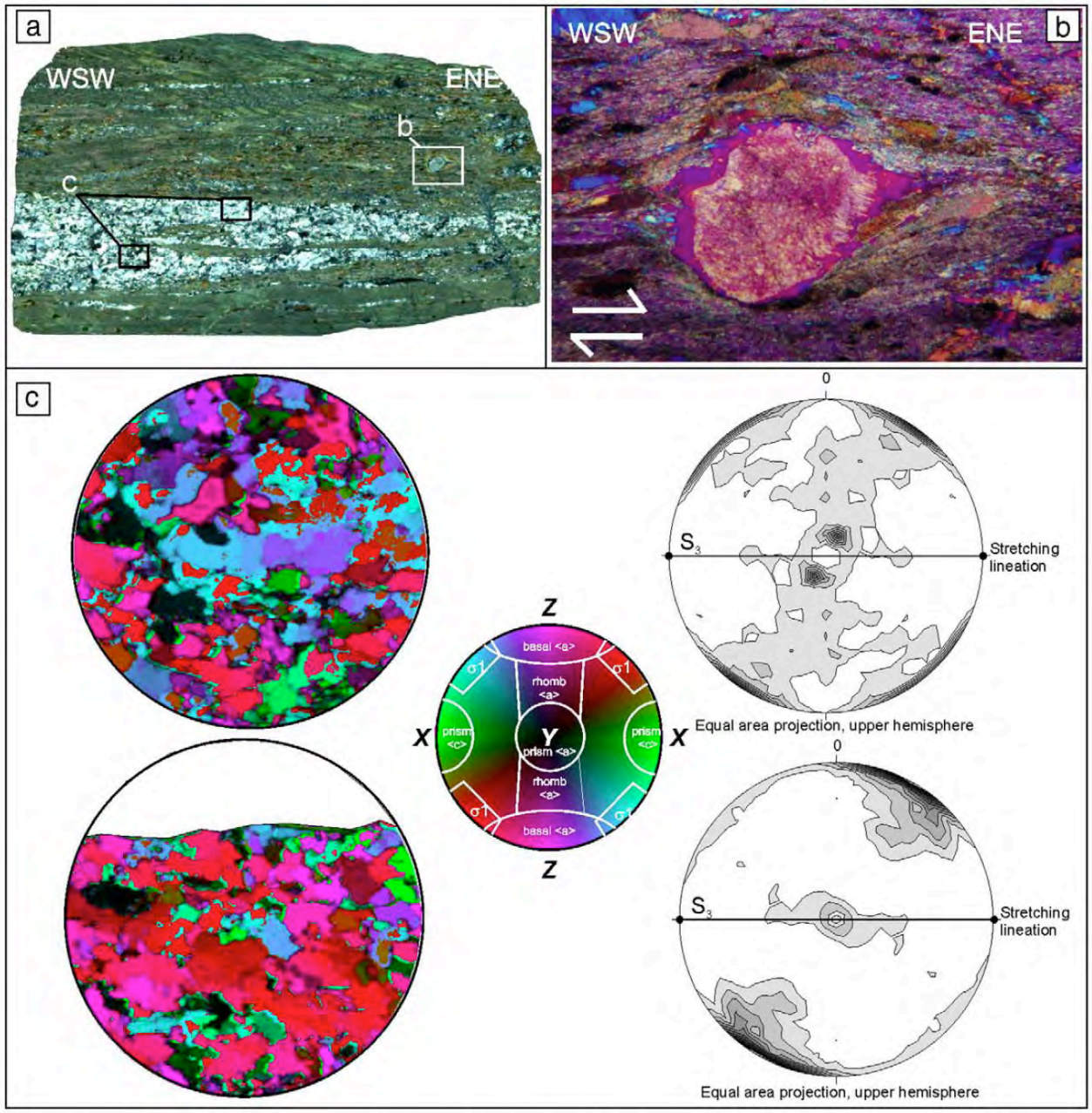

Fig. 6. Syn- to late-mylonitic textural features representative of greenschist facies up to amphibolite facies conditions develop during mylonitic stage. (a) Thin section image of mylonitic sample, with location of some representative syn- to late-mylonitic textural domains (high resolution scan: crossed polars), (b) Evidence of late dynamic growth of oligoclase rim over former plagioclase porphyroclast (crossed polars, λ plate inserted); (c) Distribution of Lattice Preferred Orientation (LPO) pattern of two representative quartz-rich domains plotted on AVA diagrams inferred via StereoNett 2.0 software (Duyster, 1996) by colour coding of reported look-up table. Left: colour-coded images of selected quartz domains (see Appendix B for explanation). Centre: colour coding scheme of look-up table with orientation of optical indicatrix axes (XYZ) and activation scheme of slip systems (see also Table 2). Right: quartz *c*-axis contour plots.

Table 4
Comparison between observed and predicted mineral assemblages and *P–T* constraints on pseudosections.

Sample		MA271		
Pseudosection: Fig. 8		Observed assemblages[a]	Constraining phases and *P–T* estimates	Computed assemblages
Orogenic cycle	early-M_1	Grt($Alm_{54}Grs_{30}Sps_{15}Prp_1$) + Pl($An_{34}$) + Ep($Czo_{90}$) + Qtz	Garnet inner core isopleths: ($Alm_{54}Grs_{30}Sps_{15}Prp_1$) (field A) 590 MPa 500 °C	Grt($Alm_{54}Grs_{30}Sps_{15}Prp_1$) + Pl($An_{34}$) + Zo + Qtz + Bt($Fe^2/(Fe^2+Mg)_{73}$) + Chl($Fe^2/(Fe^2+Mg)_{70}$) + Wmca($Phg_{14}$)
	late-M_1	Grt($Alm_{69}Grs_{25-26}Sps_{1-2}Prp_4$) + Pl($An_{20-22}$) + Qtz	Garnet outer core isopleths: ($Alm_{69}Grs_{25-26}Sps_{1-2}Prp_4$) + Pl($An_{20-22}$) (field B) 900 MPa 530 °C	Grt($Alm_{69}Grs_{25-26}Sps_{1-2}Prp_4$) + Pl($An_{20-22}$) + Qtz + Bt($Fe^2/(Fe^2+Mg)_{64}$) + Chl($Fe^2/(Fe^2+Mg)_{56}$) + Wmca($Phg_{21}$)
	early-M_3	Grt($Alm_{74}Sps_4Grs_4Prp_{22}$) + Pl($An_{34-36}$) + Qtz	Not found in the pseudosection	
Thermal metamorphism	M_4	Grt($Alm_{82}Sps_3Grs_3Prp_{12}$) + Bt($Fe^2/(Fe^2+Mg)_{61-64}$)	Not found in the pseudosection	
Sample		AR221		
Pseudosection: Fig. 9		Observed assemblages[a]	Constraining phases and *P–T* estimates	Computed assemblages
Orogenic cycle	M_1	Grt($Alm_{55}Grs_{14}Sps_{27}Prp_3$) + Pl($An_{39-41}$)	Garnet inner core isopleths: ($Alm_{55}Grs_{14}Sps_{27}Prp_3$) (field A′) 650 MPa 520 °C	Grt($Alm_{55}Grs_{14}Sps_{27}Prp_3$) + Pl($An_{38}$) + Zo + Qtz + Bt($Fe^2/(Fe^2+Mg)_{57}$) + Chl($Fe^2/(Fe^2+Mg)_{55}$) + Wmca($Phg_{14}$)
	late-M_1	Grt($Alm_{64}Grs_8Sps_{23}Prp_5$) + Pl($An_{35-37}$) + Wmca($Phg_{14-20}$)	Garnet outer core isopleths: ($Alm_{64}Grs_8Sps_{23}Prp_5$) (field B′) 750 MPa 590 °C	Grt($Alm_{64}Grs_8Sps_{23}Prp_5$) + Pl($An_{35}$) + Zo + Qtz + Bt($Fe^2/(Fe^2+Mg)_{45}$) + Chl($Fe^2/(Fe^2+Mg)_{41}$) + Wmca($Phg_{12}$)
	early-M_3	Grt($Alm_{52}Grs_{29}Sps_{10}Pyr_9$) + Wmca($Phg_{10-7}$)	Garnet inner core isopleths: ($Alm_{52}Grs_{29}Sps_{10}Pyr_9$) (field C′) 420 MPa 510 °C	Grt($Alm_{52}Grs_{29}Sps_{10}Pyr_9$) + Pl($An_{38}$) + Qtz + Bt($Fe^2/(Fe^2+Mg)_{60}$) + Chl($Fe^2/(Fe^2+Mg)_{56}$) + Wmca($Phg_8$)
Thermal metamorphism	M_4	Grt($Alm_{52}Grs_{10}Sps_{29}Prp_8$) + St + And + Bt($Fe^2/(Fe^2+Mg)_{62}$)	Not found in the pseudosection	
Sample		GR164		
Pseudosection: Fig. 11		Observed assemblages[a]	Constraining phases and *P–T* estimates	Computed assemblages
Orogenic cycle	Early- stages	Grt($Alm_{54}Grs_{18}Sps_{24}Prp_4$) + Ab + Wmca($Phg_{16-19}$)	Not found in the pseudosection	
	Late-retrograde	Pl(An_{26}) + Wmca(Phg_{6-9}) + Chl($Fe^2/(Fe^2+Mg)_{56-59}$)	Syn-mylonitic assemblage in porphyroclastic pressure shadow domains: Pl(An_{26}) + Wmca(Phg_{6-9}) + Chl($Fe^2/(Fe^2+Mg)_{56-59}$) (field A″) 300 MPa 490 °C	Pl(An_{26}) + Wmca(Phg_7) + Chl($Fe^2/(Fe^2+Mg)_{59}$) + Bt($Fe^2/(Fe^2+Mg)_{65}$)
Sample		GR166		
Pseudosection: Fig. 12		Observed assemblages[a]	Constraining phases and *P–T* estimates	Computed assemblages
Orogenic cycle	Retrograde stages	St + Wmca(Phg_{10-5}) + Bt($Fe^2/(Fe^2+Mg)_{61-64}$)	Not found in the pseudosection	
Thermal metamorphism	Peak	Bt($Fe^2/(Fe^2+Mg)_{61-64}$) + Crd($Mg/(Fe^2+Mg)_{45-47}$) + Sil	Static porphyroblastic mineralogical growth: Bt($Fe^2/(Fe^2+Mg)_{61-64}$) + Crd($Mg/(Fe^2+Mg)_{45-47}$) (field A‴) 300 MPa 685 °C	Bt($Fe^2/(Fe^2+Mg)_{65}$) + Crd($Mg/(Fe2+Mg)_{47}$) + Sil Pl(An_{21})
	Late retrograde	And + Pl(An_{24}) + Chl($Fe^2/(Fe^2+Mg)_{56-59}$)	Retrograde pseudomorphic assemblage: Pl(An_{24}) + Chl($Fe^2/(Fe^2+Mg)_{56-59}$) (field B‴) 150 MPa 500 °C	And + Pl(An_{24}) + Chl($Fe^2/(Fe^2+Mg)_{57}$) + Bt($Fe2/(Fe^2+Mg)_{69}$) + Wmca(Phg_3)

[a] Observed mineral assemblages have been recalculated: a) Garnet, considering all iron as FeO (i.e. on the basis of Alm–Sps–Grs–Prp endmembers); b) White mica, considering the $Si_{a.p.f.u.}$ variable from 3.0 (i.e. Muscovite) to 4.0 (i.e. Celadonite), expressed as phengite content (e.g. $Si_{a.p.f.u.}$ 3.30 = Phe_{30}); c) Chlorite and biotite expressed as $Fe^2/(Fe^2+Mg)$ ratio and d) cordierite expressed as $Mg/(Fe^2+Mg)$.

Angie et al 2010

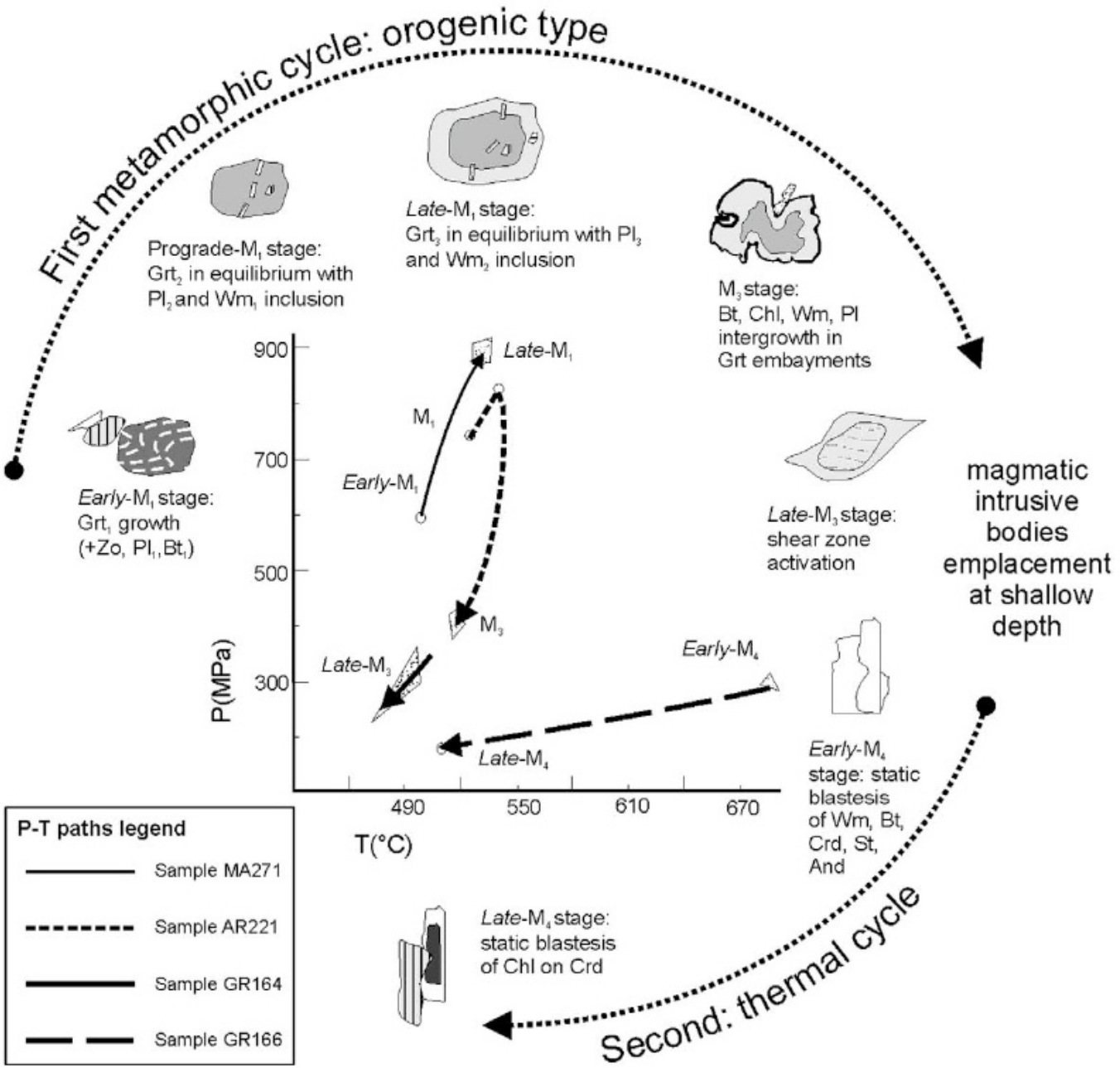

Fig. 13. Integration of estimated *P–T* constraints and reconstruction of *P–T* path (thick black arrows) of Mammola Paragneiss Complex, illustrated by multi-stage mineral growth scheme representing discrete stages of Hercynian tectono-metamorphic history.

Angie et al 2010

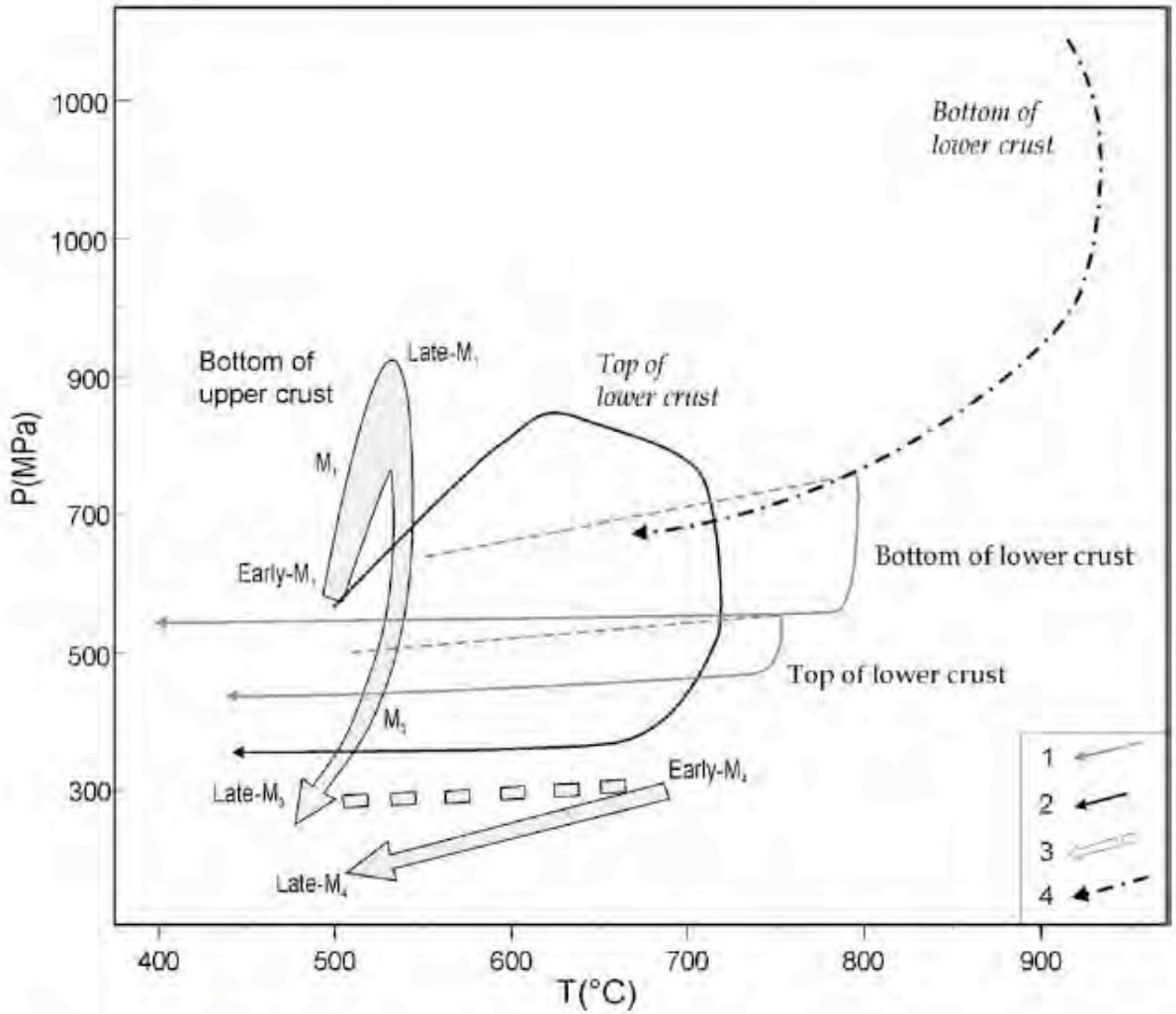

Fig. 14. Pressure–temperature trajectories reconstructed by various authors for parts of Serre Massif crustal section: 1) *P–T* paths related to rocks belonging to uppermost and lowermost parts of lower crust (after Schenk, 1989); 2) *P–T* path of uppermost part of lower crustal segment (after Acquafredda et al., 2006); 3) *P–T* path reconstruction considering thermobarometric estimates of this paper for bottom of upper crust; 4) *P–T* path of lowermost part of lower crustal segment (after Acquafredda et al., 2008).

Angie
et al 2010

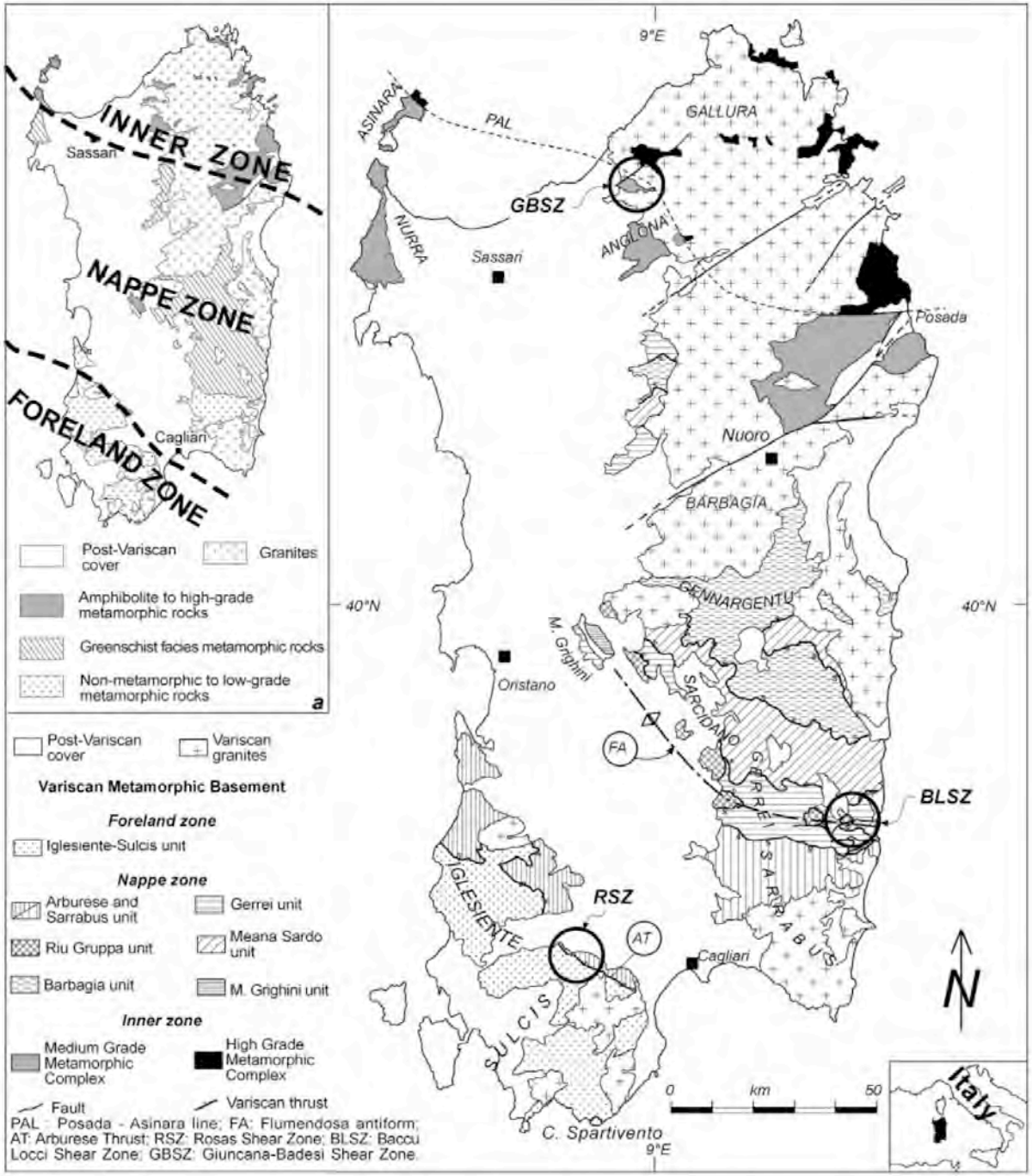

Figure 1. Geological sketch map of the Variscan basement of Sardinia, the black circles indicate the study areas cited in the text. (a) Tectonic and metamorphic zoning of the Variscan basement of Sardinia.

Casini et al 2010

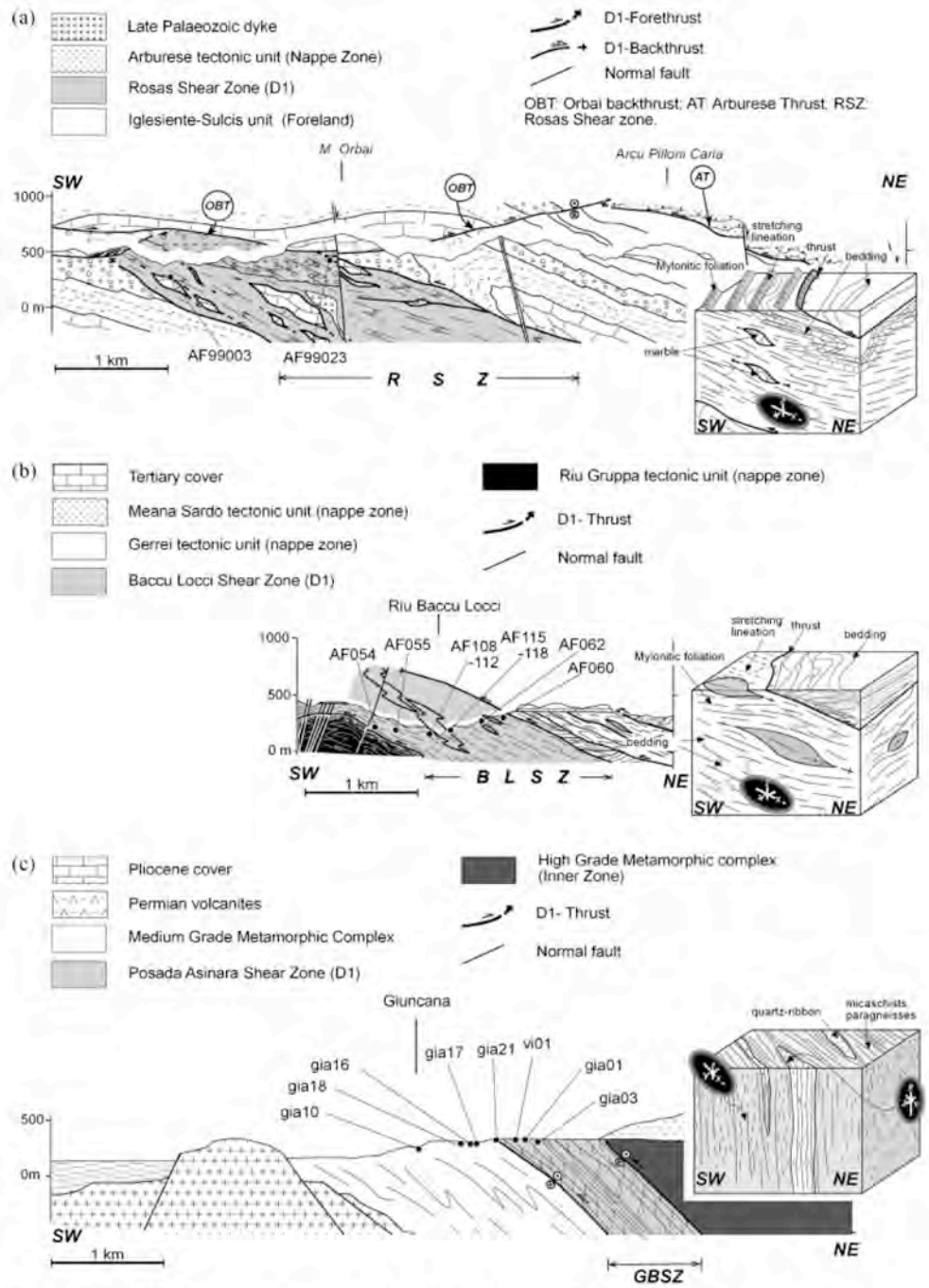

Figure 2. Geological cross-sections across the studied shear zones in the Sardinian Variscides, with location of the studied samples. Schematic fabric diagrams on the right are not to scale. (a) Rosas Shear Zone (RSZ) between the Nappe zone and the foreland; (b) Baccu Locci Shear Zone (BLSZ) inside the Nappe zone; (c) Giuncana-Badesi Shear Zone (GBSZ) in the Inner zone between the high-grade and the medium-grade metamorphic complexes.

Casini et al 2010

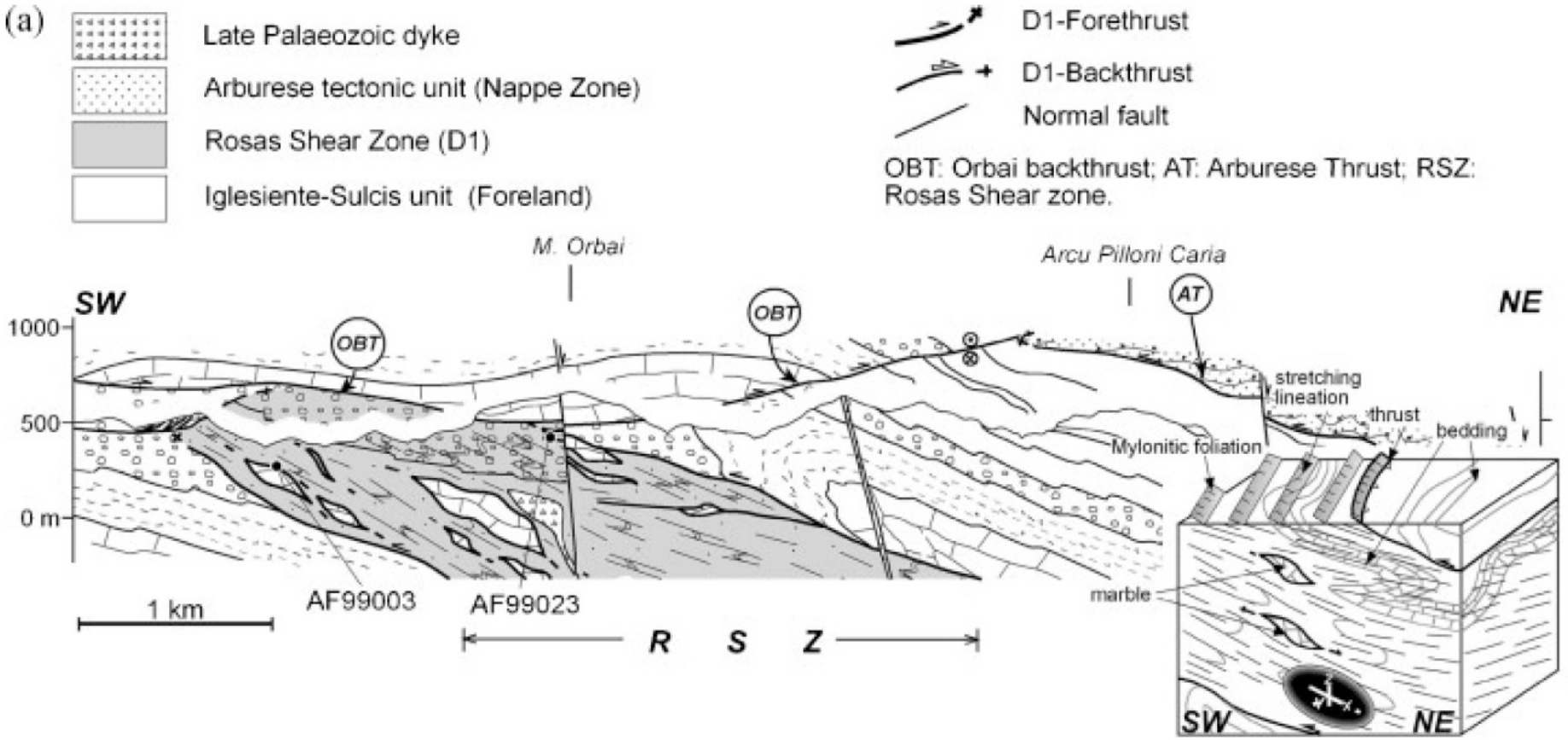

Figure 2. Geological cross-sections across the studied shear zones in the Sardinian Variscides, with location of the studied samples. Schematic fabric diagrams on the right are not to scale. (a) Rosas Shear Zone (RSZ) between the Nappe zone and the foreland; (b) Baccu Locci Shear Zone (BLSZ) inside the Nappe zone; (c) Giuncana-Badesi Shear Zone (GBSZ) in the Inner zone between the high-grade and the medium-grade metamorphic complexes.

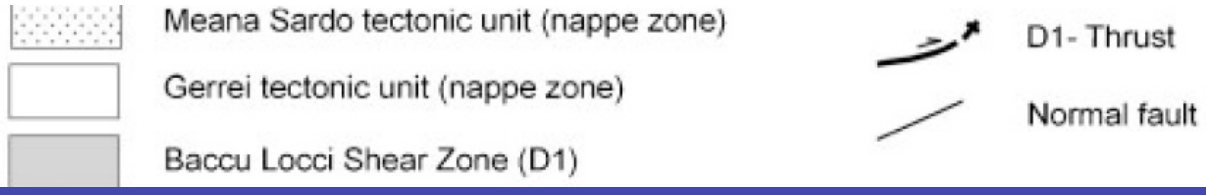

Casini et al 2010

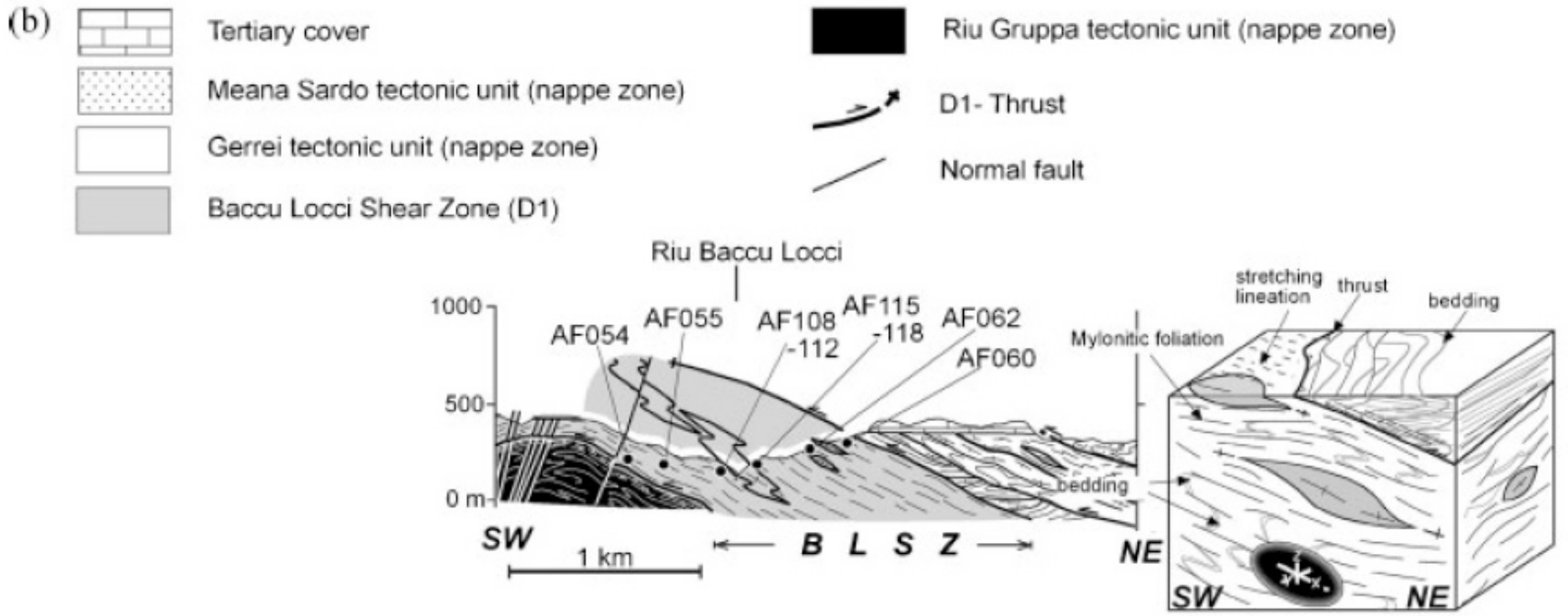

Figure 2. Geological cross-sections across the studied shear zones in the Sardinian Variscides, with location of the studied samples. Schematic fabric diagrams on the right are not to scale. (a) Rosas Shear Zone (RSZ) between the Nappe zone and the foreland; (b) Baccu Locci Shear Zone (BLSZ) inside the Nappe zone; (c) Giuncana-Badesi Shear Zone (GBSZ) in the Inner zone between the high-grade and the medium-grade metamorphic complexes.

Casini et al 2010

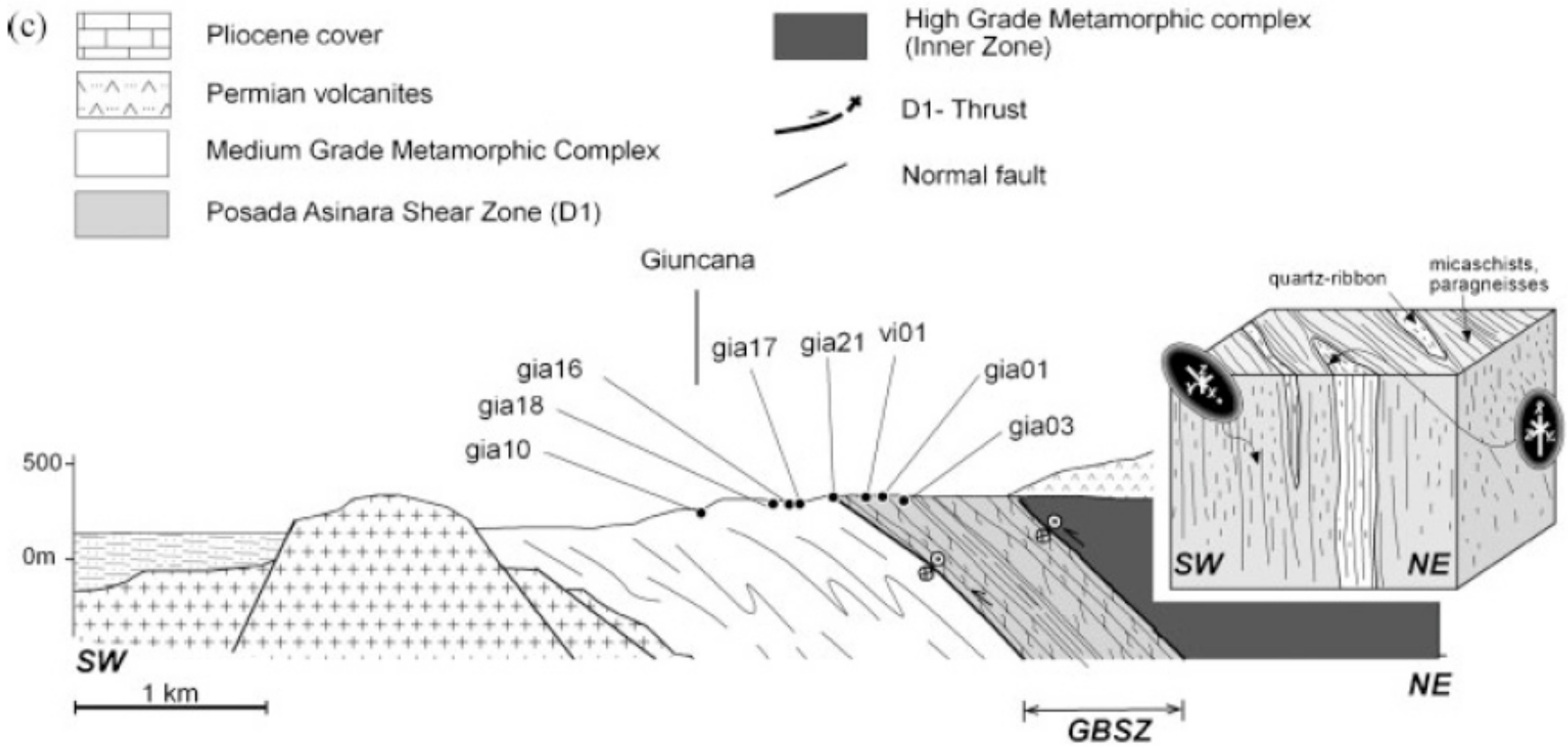

Figure 2. Geological cross-sections across the studied shear zones in the Sardinian Variscides, with location of the studied samples. Schematic fabric diagrams on the right are not to scale. (a) Rosas Shear Zone (RSZ) between the Nappe zone and the foreland; (b) Baccu Locci Shear Zone (BLSZ) inside the Nappe zone; (c) Giuncana-Badesi Shear Zone (GBSZ) in the Inner zone between the high-grade and the medium-grade metamorphic complexes.

Casini et al 2010

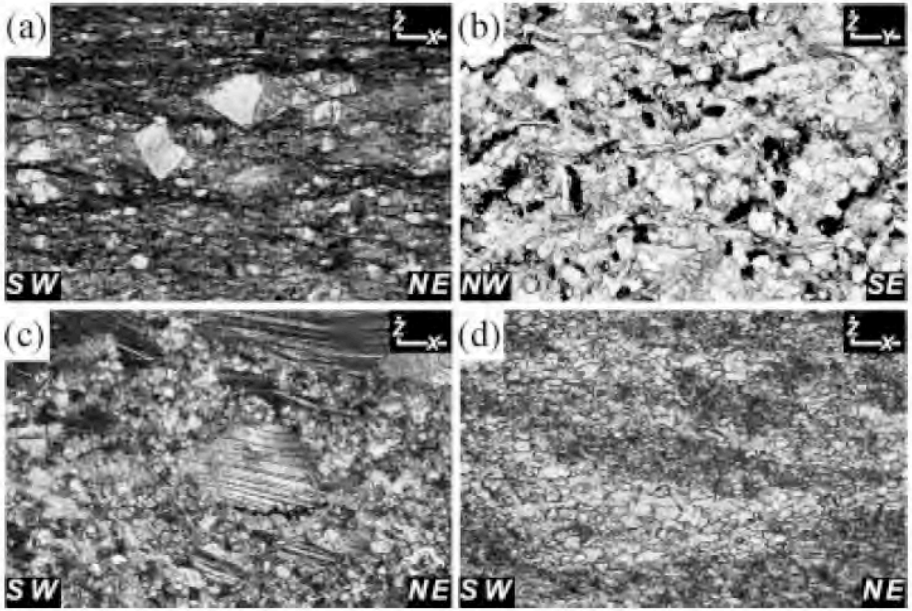

Figure 3. Microstructure of the RSZ mylonites, plane polarized light. The width of photomicrographs is 1.7 mm, the orientation relative to both the structural and geographic reference systems is specified within each picture, (a) quartz grains with partly dissolved boundaries, meta-sandstones; (b) detrital muscovite flakes within a poorly deformed level rich in Fe-oxides, meta-sandstones; (c) coarse-grained calcite-ribbons. The calcite grains in the centre of the picture is mantled by a finer-grained matrix of apparently recrystallized grain; (d) texture in calc-mylonites: extremely fine-grained layers of dynamically recrystallized calcite grains.

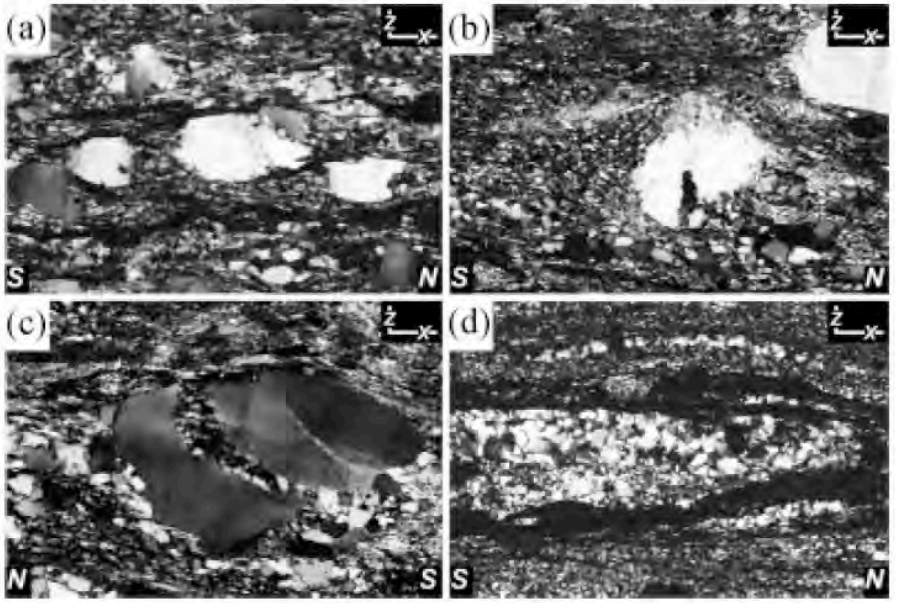

Figure 4. Microstructure of the BLSZ mylonites; width of photomicrographs is 1.7 mm, crossed polarizer. The orientation relative to both the structural and geographic reference systems is specified within each picture, (a) stretched quartz grains with optically visible sub-grain boundaries and undulose extinction; (b) core-and-mantle textures around quartz porphyroclast, centre of the photograph; (c) through-going micro-shear zone; (d) high-strained sample (sample AF062): quartz porphyroclasts are almost completely recrystallized and transformed into polycrystalline ribbons, alternating with dark seams rich in Fe-oxides, muscovite and secondary chlorite.

Casini et al 2010

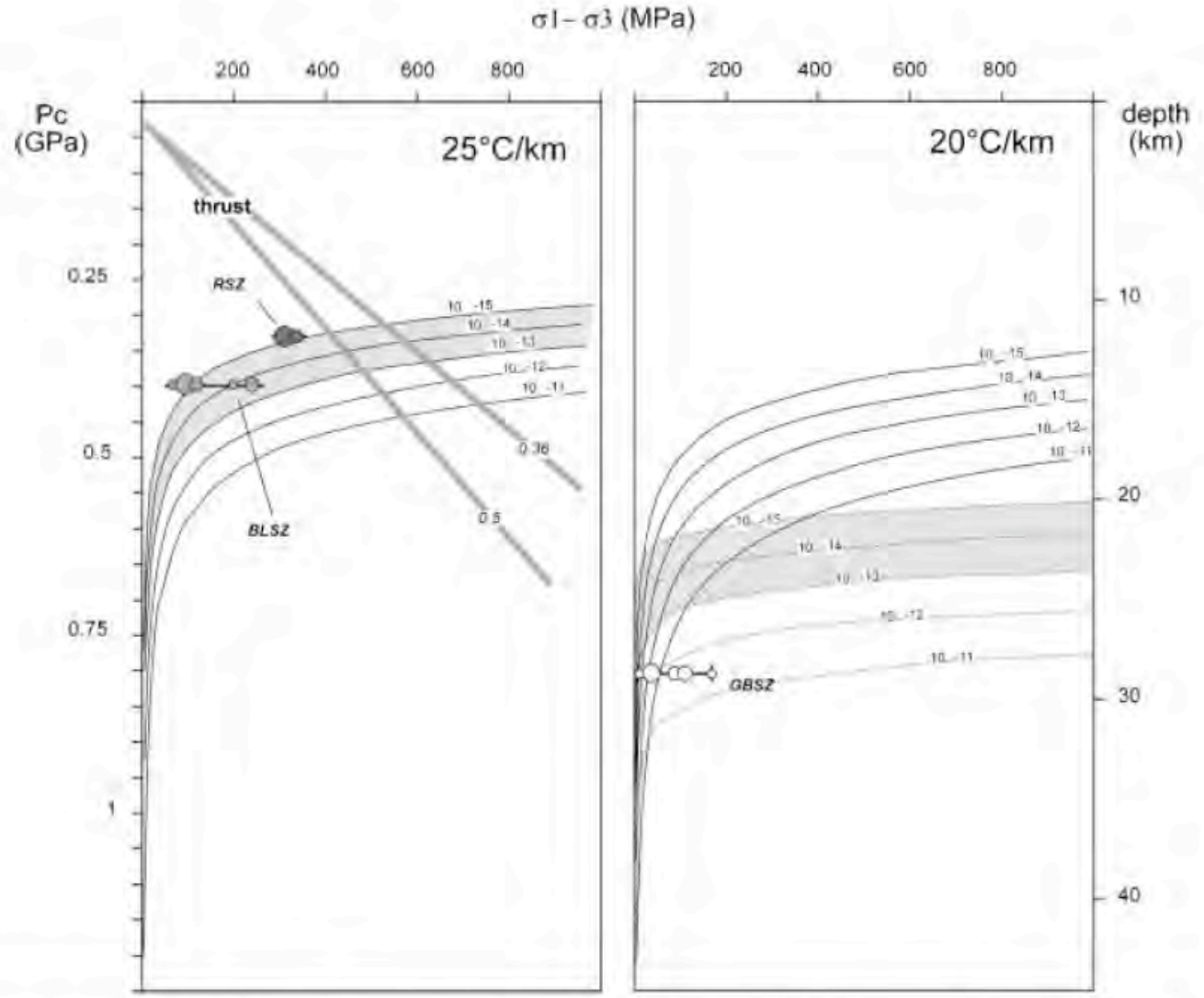

Figure 7. Strength/depth profiles with respect to D1 deformation, (sub-greenschist to greenschist level, geothermal gradient of 25° km^{-1}. The grey lines indicate the frictional strength of the upper crust in a thrust regime, for a pore-fluid pressure value of 0.36 and 0.5, respectively. Dark curves indicate the viscous strength at different strain rates (s^{-1}), calculated assuming dislocation creep of wet quartz (data by Gleason and Tullis, 1995); the shaded area represents the field of geologically reasonable strain rates (Pfiffner and Ramsay, 1982). The stress profiles calculated in the RSZ and BLSZ are indicated, upper-greenschist to amphibolite level, geothermal gradient of 20° km^{-1}. Dark curves indicate the viscous strength at different strain rates (s^{-1}), calculated assuming dislocation creep of wet quartz (data by Gleason and Tullis, 1995). The dashed curves indicate the viscous strength of the crust calculated assuming diffusion creep of (data by Rutter and Brodie, 2004), the shaded area represents the field of geologically reasonable strain rates (following Pfiffner and Ramsay, 1982). The stress profiles calculated from the GBSZ mylonites is indicated.

Casini et al 2010

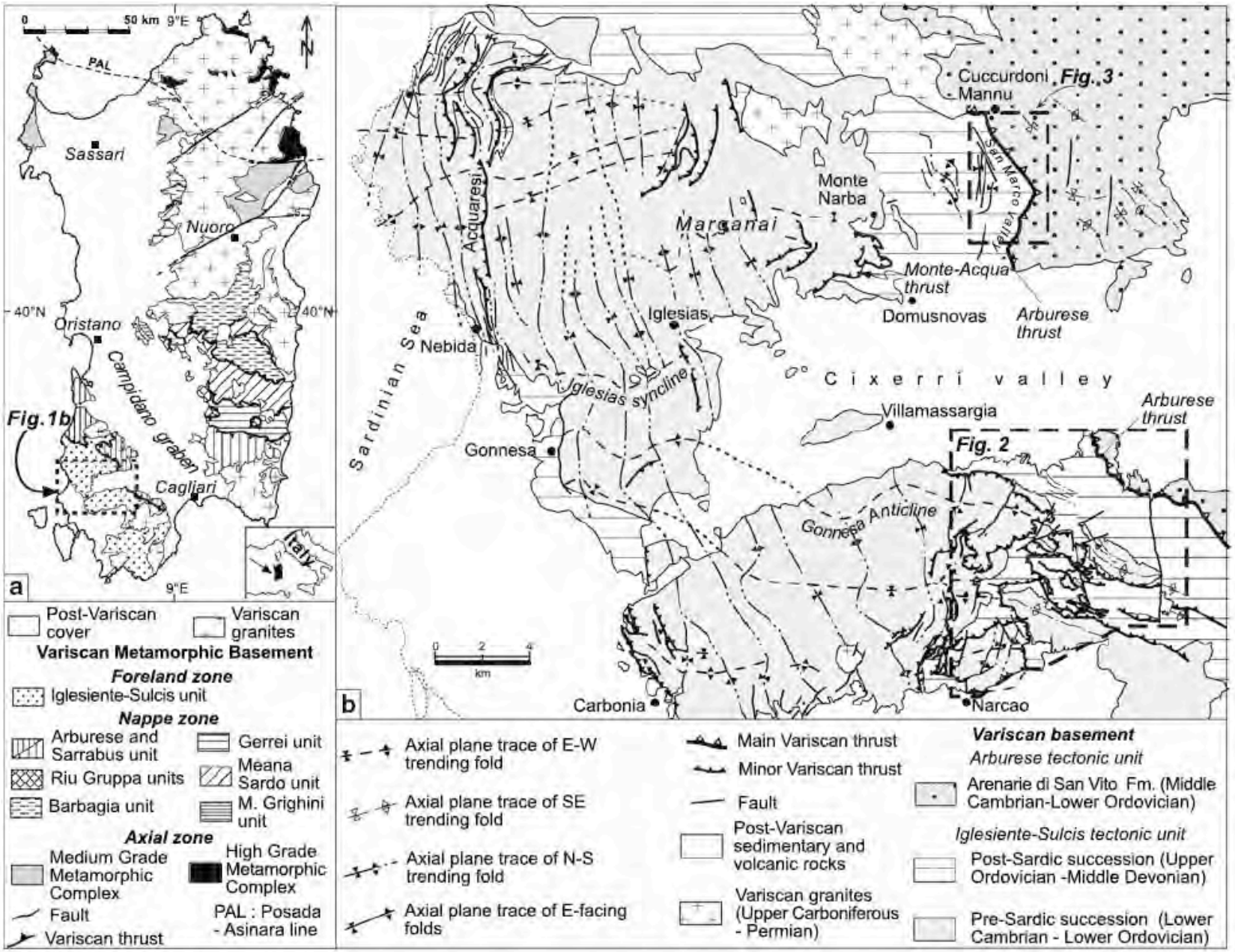

Fig. 1 a Geological sketch map of SW-Sardinia; b tectonic sketch map of N-Sulcis Iglesiente area, *dashed squares* show the location of geological map in Figs. 2 and 3

Funedda 2009

Table 1 Summarized table of the Variscan structures elements recognized in the field, main structures at the map-scale and relative deformative phases and shortening direction

Structural elements mapped	Main structures	Deformative phases	Shortening direction
E–W-trending folds without axial plane cleavage (A_1)	Gonnesa Anticline (GA)	1° Variscan phase	N–S
SE-trending folds with axial plane cleavage (S_{2a}, A_{2a}, L_{2a})	Rosas Shear Zone (RSZ) Perdu Sanna (PSA) and Bega Rosas (BRA) anticlines	2° Variscan phase	NE–SW
Forethrust (W-warding), N–S-trending folds with axial plane cleavage (S_{2b}, A_{2b})	Arburese Thrust (AT), Genna Pira folds, Monte Ettoi anticline (EA)		E–W
Backthrust (E-warding), mylonitic foliation, E-facing folds without axial plane cleavage (S_m, A_{2c}, L_{2c})	Orbai (OBT) and Monte Atzei (ABT) backthrusts		E–W
Low-angle and high-angle normal faults	Monte Ettoi fault, Normal faults in the Planeserra-Orbai area	Late orogenic extension	?

Deformation events and related structures in the Variscan foreland of SW-Sardinia

A fold axes, *S* tectonic foliations, *L* stretching lineation (lower cases distinguish different tectonic phases)

Funedda 2009

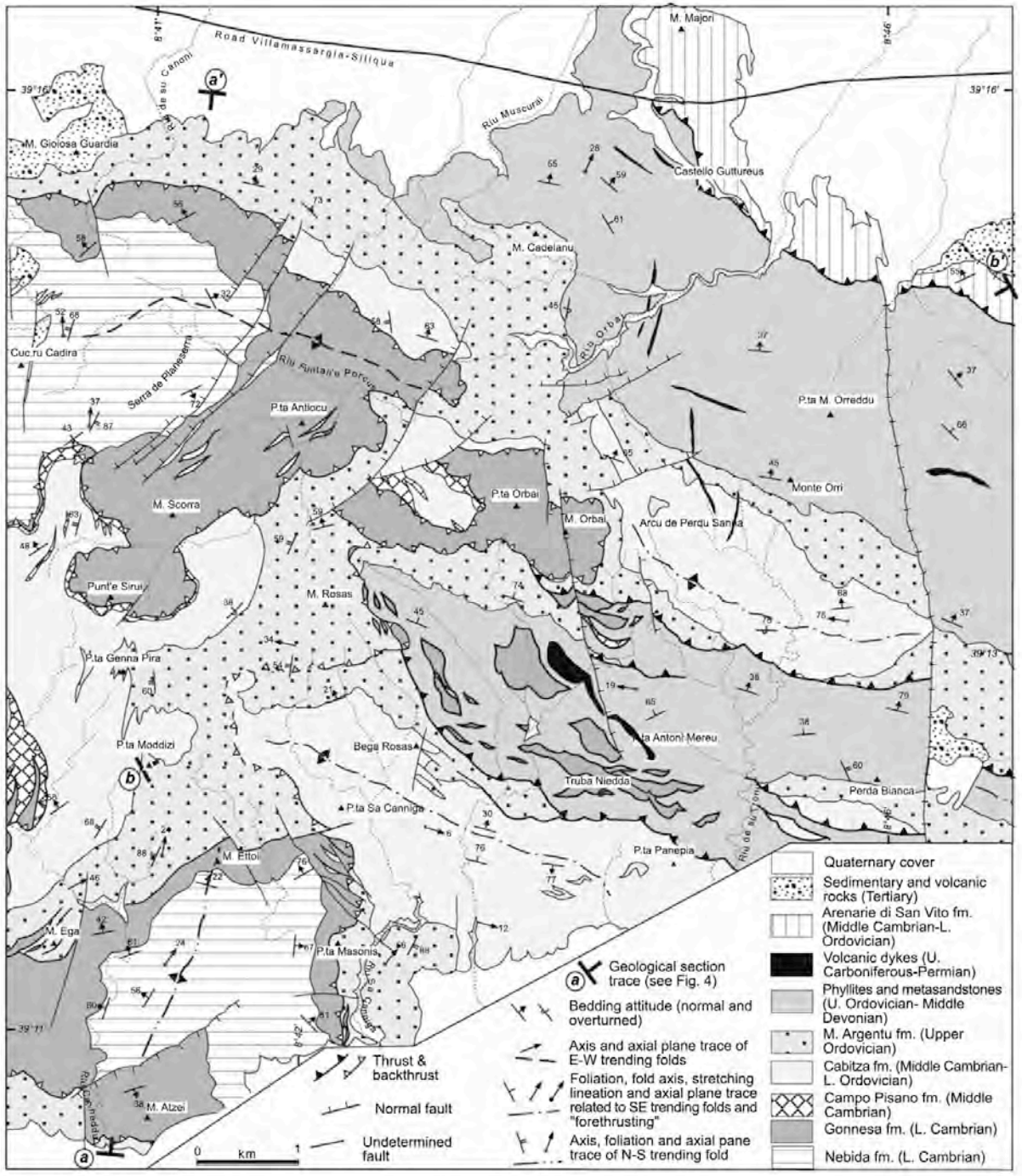

Fig. 2 **a** Geological map of the Orbai-Rosas area; **b** structural map of the Orbai-Rosas area (*grey dotted lines* are rivers)

Funedda 2009

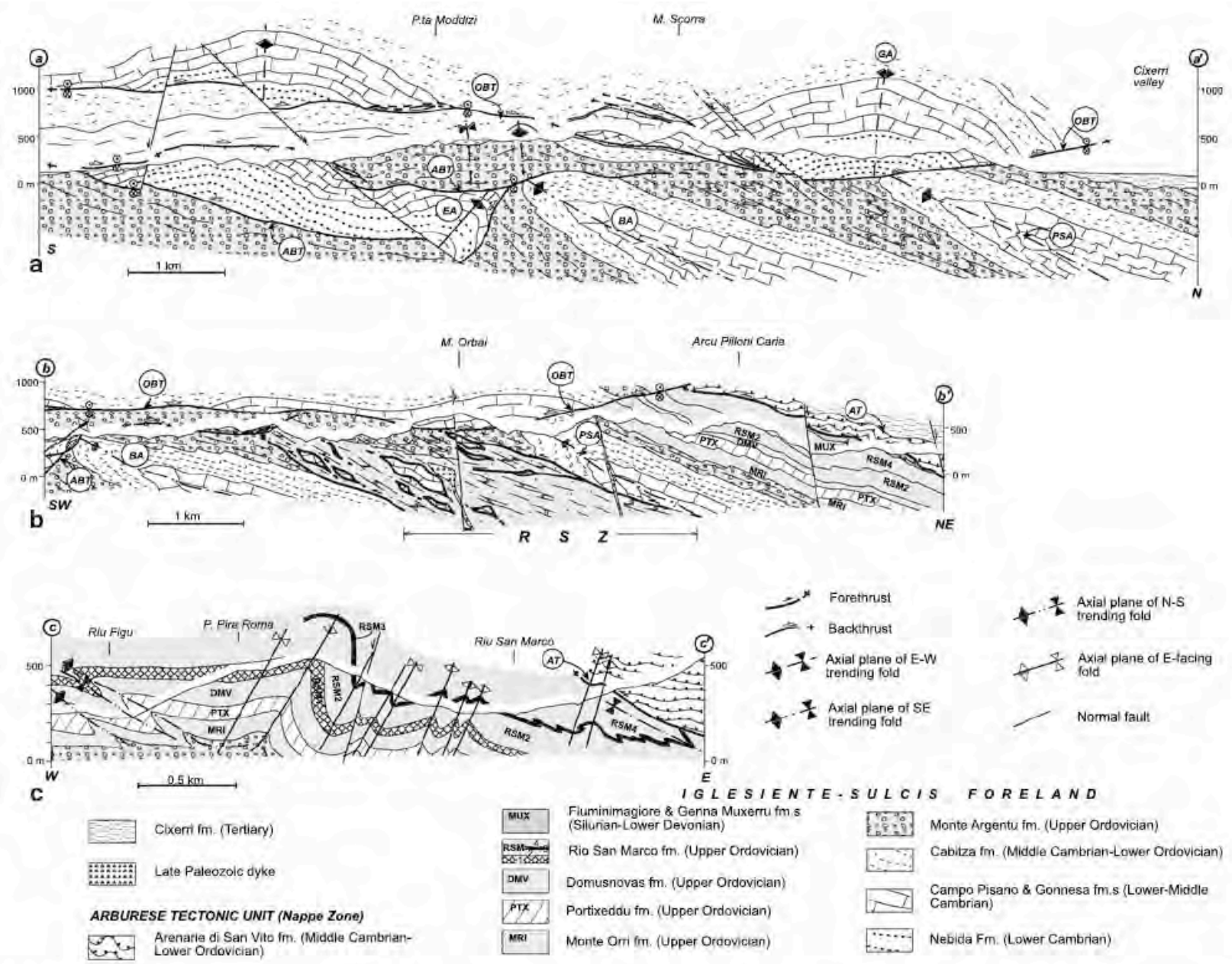

Fig. 4 Geological section of **a** Orbai area (section trace in Fig. 2a), **b** Rosas area (section trace in Fig. 2a), **c** Rio San Marco Valley (section trace in Fig. 3)

Funedda 2009

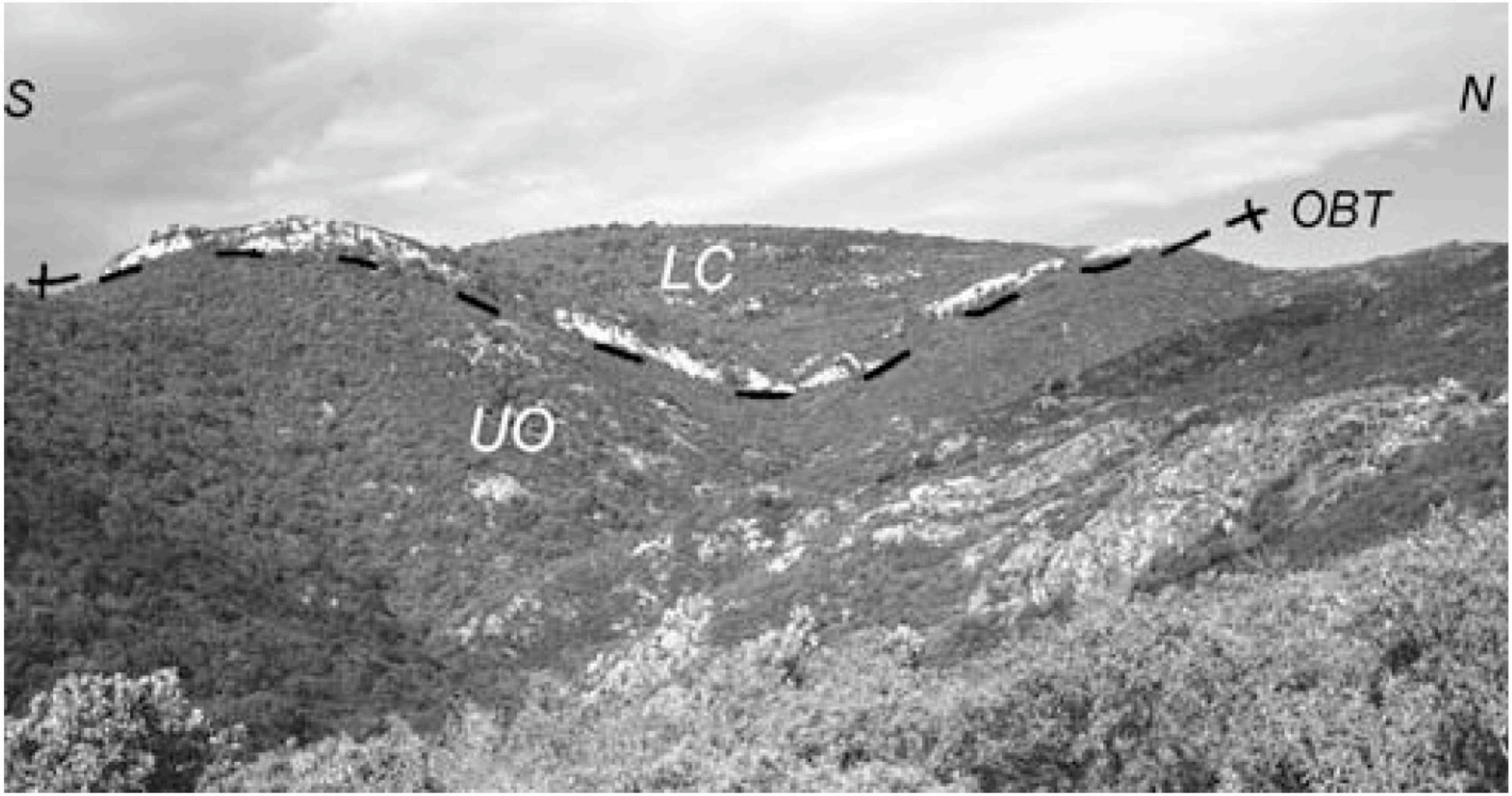

Fig. 11 Panoramic view of the frontal side of the Orbai backthrust (*dashed line*, *OBT*). *LC* Lower Cambrian limestone, *UO* Upper Ordovician slate. View from Punta Is Casiddu towards W

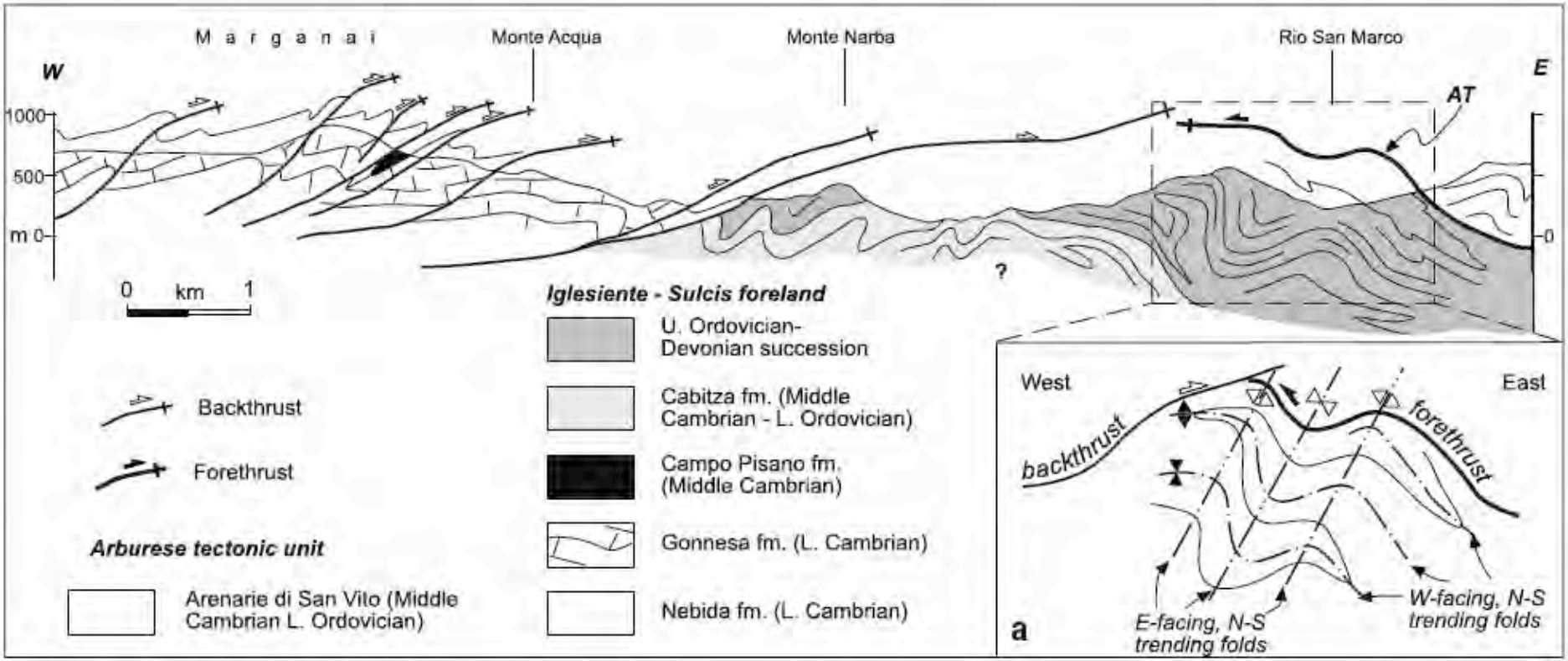

Fig. 15 Schematic geological section across the Marganai region, showing cross-cutting relationships between forethrust and backthrust. In the "quasi-triangle zone" shaped by the Monte Acqua backthrust system and the Arburese forethrust (*AT*) the interference between thrusts, N–S-trending folds with both W- and E-facing direction results in a complex architecture (see sketch in *inset* a)

Funedda 2009

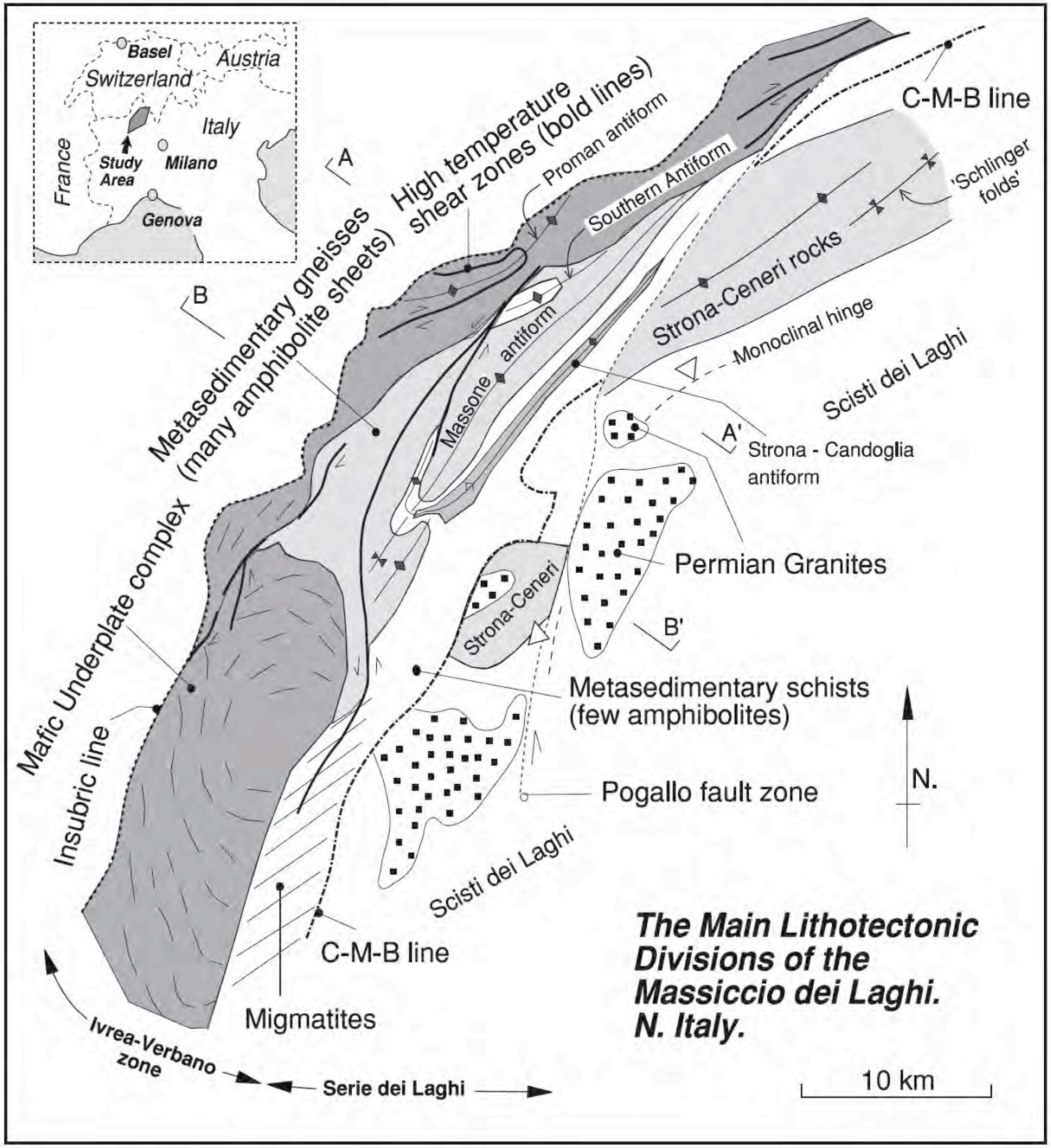

Fig. 1. Sketch map showing the main lithotectonic divisions of the Massiccio dei Laghi. A−A′ and B−B′ indicate the positions of the Valle d'Ossola and Val Strona sections through the region shown in Figs. 9 and 3, respectively. C-M-B line = the Cossato-Mergozzo-Brissago line, the tectonic contact between the Ivrea-Verbano and Serie dei Laghi terrains. Inset map shows the location of the Massicio dei Laghi in northern Italy.

Rutter et al 2009

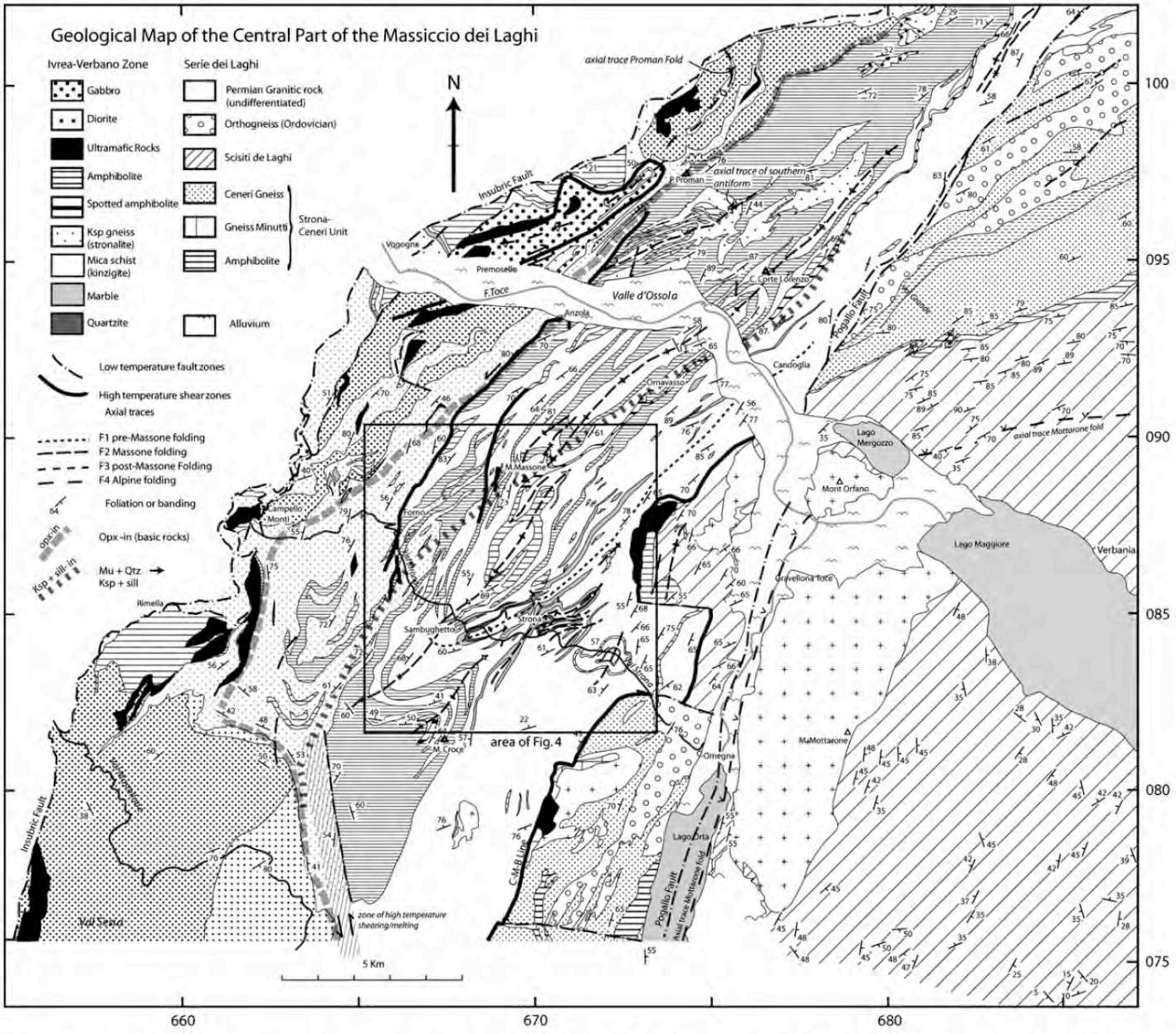

Fig. 2. Geological map of the central part of the I-V zone and the adjacent Serie dei Laghi. The central part of the map represents the results of new geological mapping, the north and western part is drawn from Rutter et al. (1993) and Evans (1995), the north from Schmid (1967), to the south from Snoke et al. (1999) and the Serie dei Laghi from the work of Boriani and Burlini (1994). In the south-east of the map note the change in dip of the main foliation on either side of the Mottarone granite pluton, from gently undulating in the south-east to near vertical to the north-west, in common with the near-vertical attitude of most of the rocks of the I-V zone. The positions shown of the main metamorphic isograds are based on Zingg (1980). Grid numbers correspond to the Swiss National (1963) Grid.

Rutter et al 2009

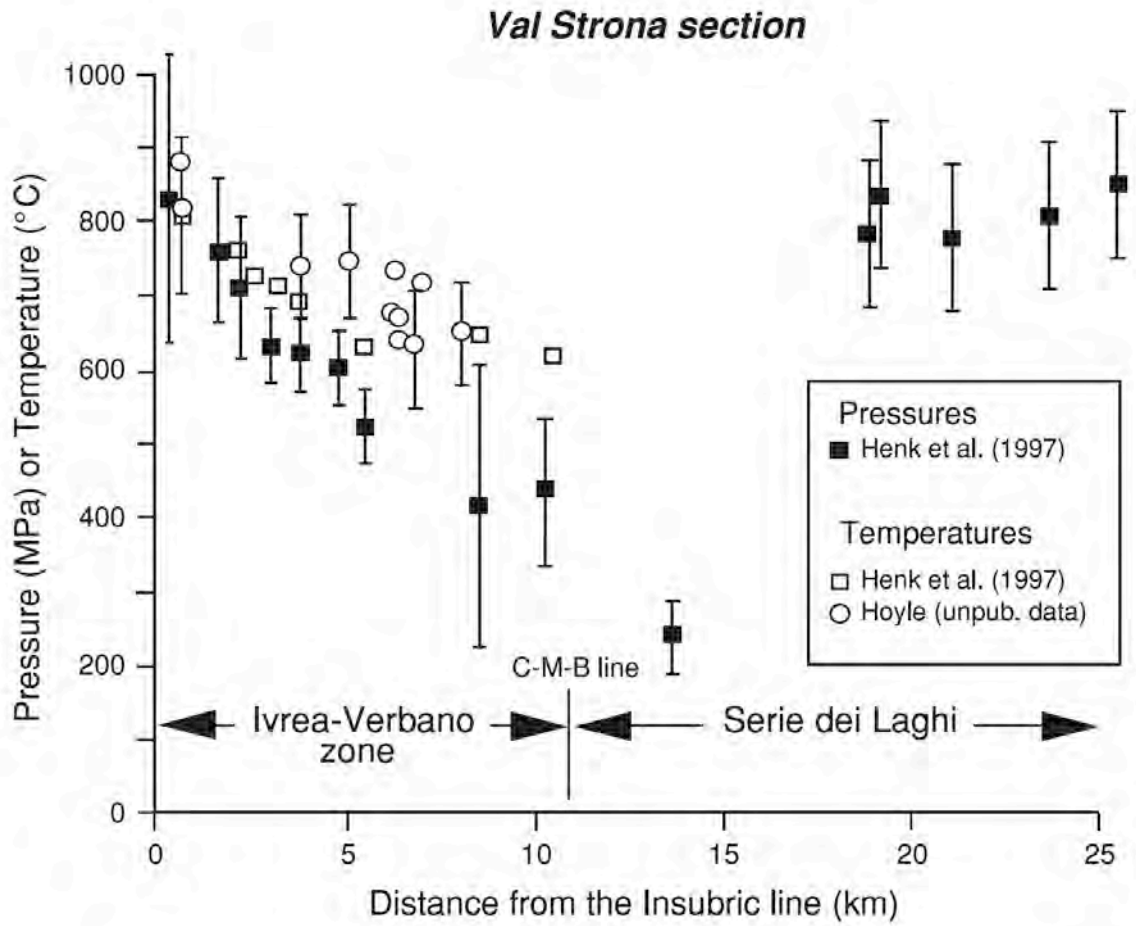

Fig. 3. Summary diagram showing paleotemperature and pressure estimates along the Val Strona transect (B–B′ on Fig. 1). Note the marked contrast between paleopressures in the Serie dei Laghi and the Ivrea-Verbano zone, and the way in which both pressure and temperature increase to the NW (inferred greater depths) in the Ivrea-Verbano zone. The steepness of the geobaric gradient is attributable to the Permian stretching and thinning the region has undergone. Unpublished thermometry data by Hoyle used the garnet–biotite geothermometer in pelites, and garnet–clinopyroxene (Ellis and Green, 1979) and amphibole–plagioclase (Blundy and Holland, 1990) in metabasic rocks.

Rutter et al 2009

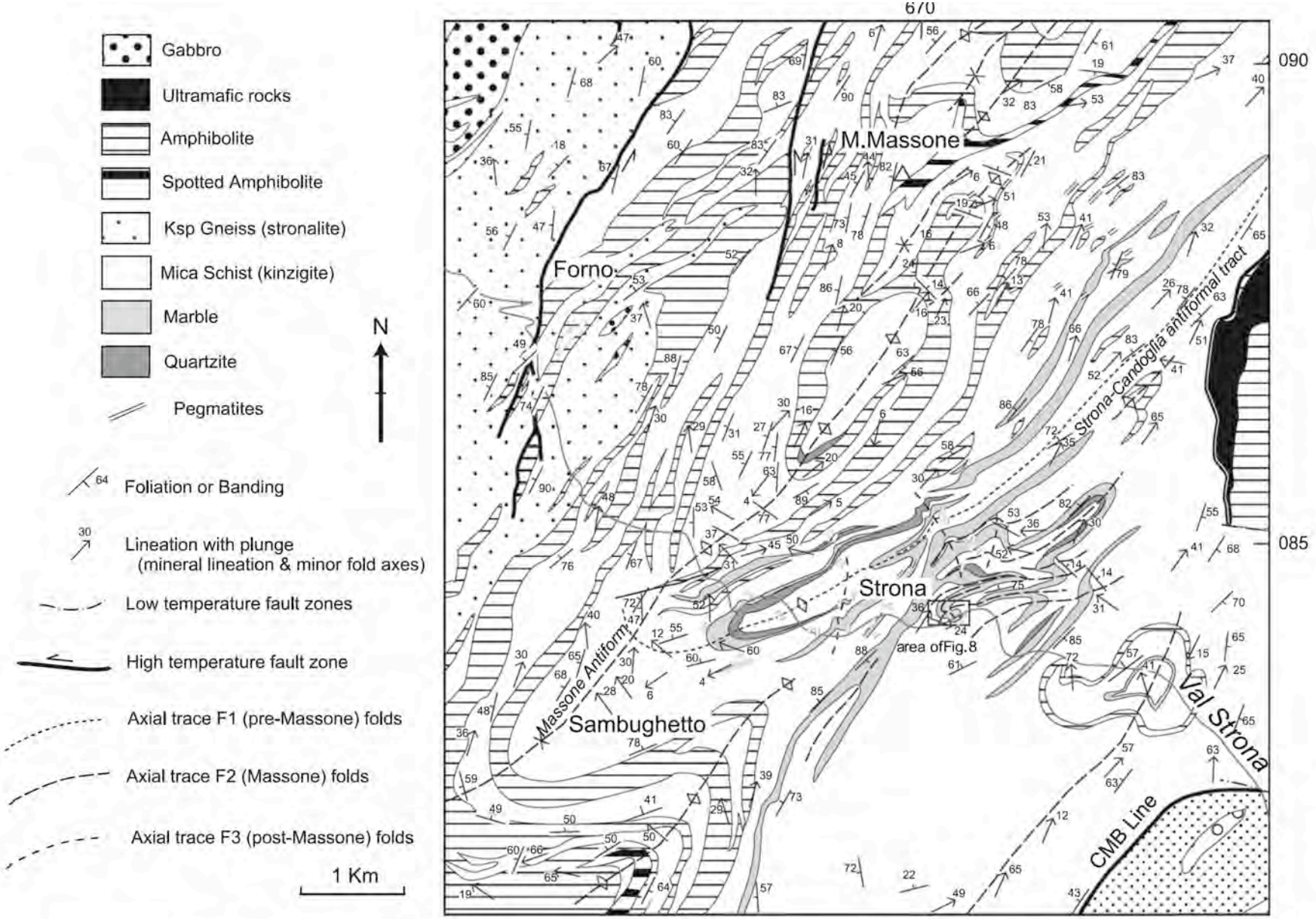

Fig. 4. Detail of the central part of Fig. 2, showing the relationships between the structure of the Massone folding and the earlier Strona-Candoglia antiformal syncline in Val Strona where they are particularly well displayed. Plunge arrows show how the early mineral lineations and fold axes are folded around the hinge of the Massone Antiform in the southern part of the map where the Massone Antiform plunges vertically. An enlarged map of the area to the east of Strona village (indicated) is shown in Fig. 8. The spotted amphibolite is distinctive through the occurrence of plagioclase rims around garnet prophyroblasts.

Rutter et al 2009

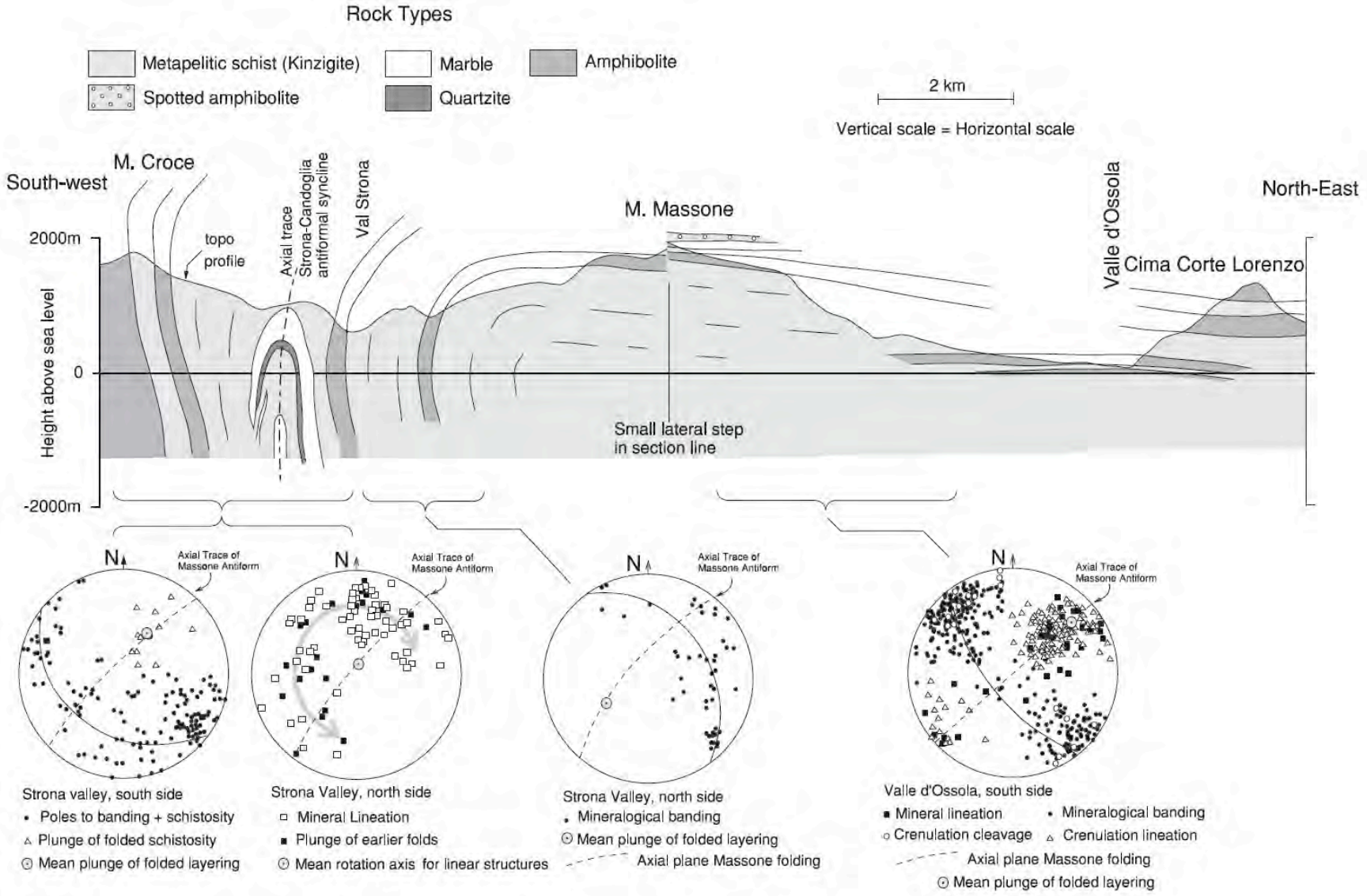

Fig. 5. Geological cross-section drawn parallel to the axial plane of the main Massone Antiform, showing the marked plunge culmination between M. Massone and Val Strona. The Massone folding refolds earlier major folds, principally the (locally steeply plunging) antiformal core of the Strona-Candoglia antiform, whose profile cuts across the axial plane of the Massone folding immediately SW of Strona valley. The equal-area, lower-hemisphere projections of data up to 2 km on either side of the Massone Antiform axial trace show how the attitude of layering and early schistosity changes along the axial zone of the Massone Antiform and how early fold axes and mineral lineations are folded about the hinge of the Massone Antiform where it is near vertical. The strong concentration of linear structures into a more gently NE plunging orientation towards the NE end of the section is typical of most of the northern I-V zone.

Rutter et al 2009

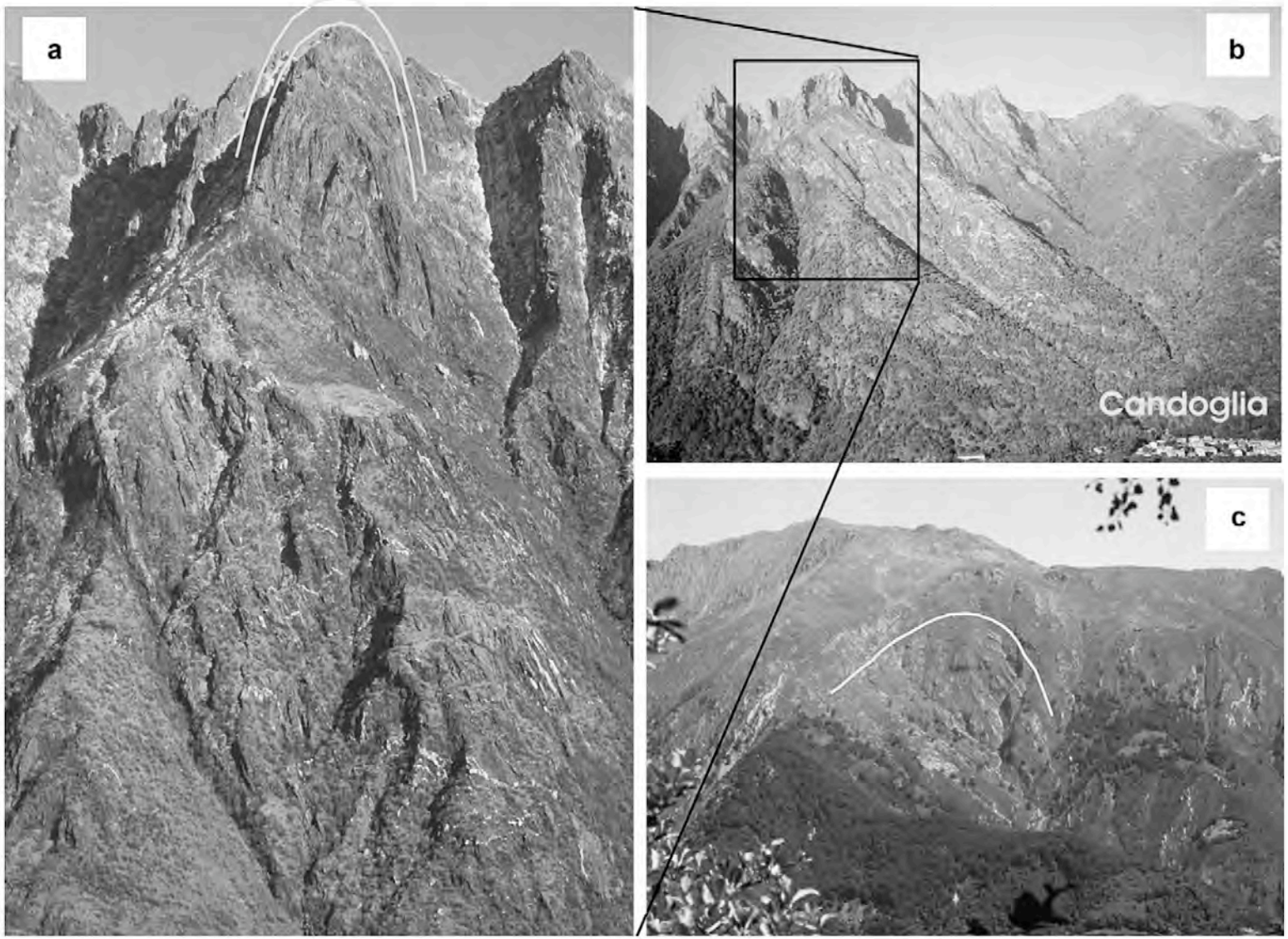

ig. 6. Photographs of the Massone Antiform as it can be seen in the field. (a) The isoclinal closure at the summit of Cima Corte Lorenzo (Fig. 2), looking NW cross the Valle d'Ossola (fold closure highlighted). Some of the swarm of small pegmatite bodies (Fig. 4) that cut the layering can just be distinguished. (b) Wider ngle view including the same field of view as in (a), but showing the full 2 km relief of the Valle d'Ossola southern side, and how the fold structure becomes more pen downwards. (c) View along the axis of the Massone Antiform on the north-eastern side of the Val Strona, from M. Croce (Fig. 2). The shape of the fold has een highlighted. Note the relatively small amount of thickening of the layers in the hinge region.

Rutter et al 2009

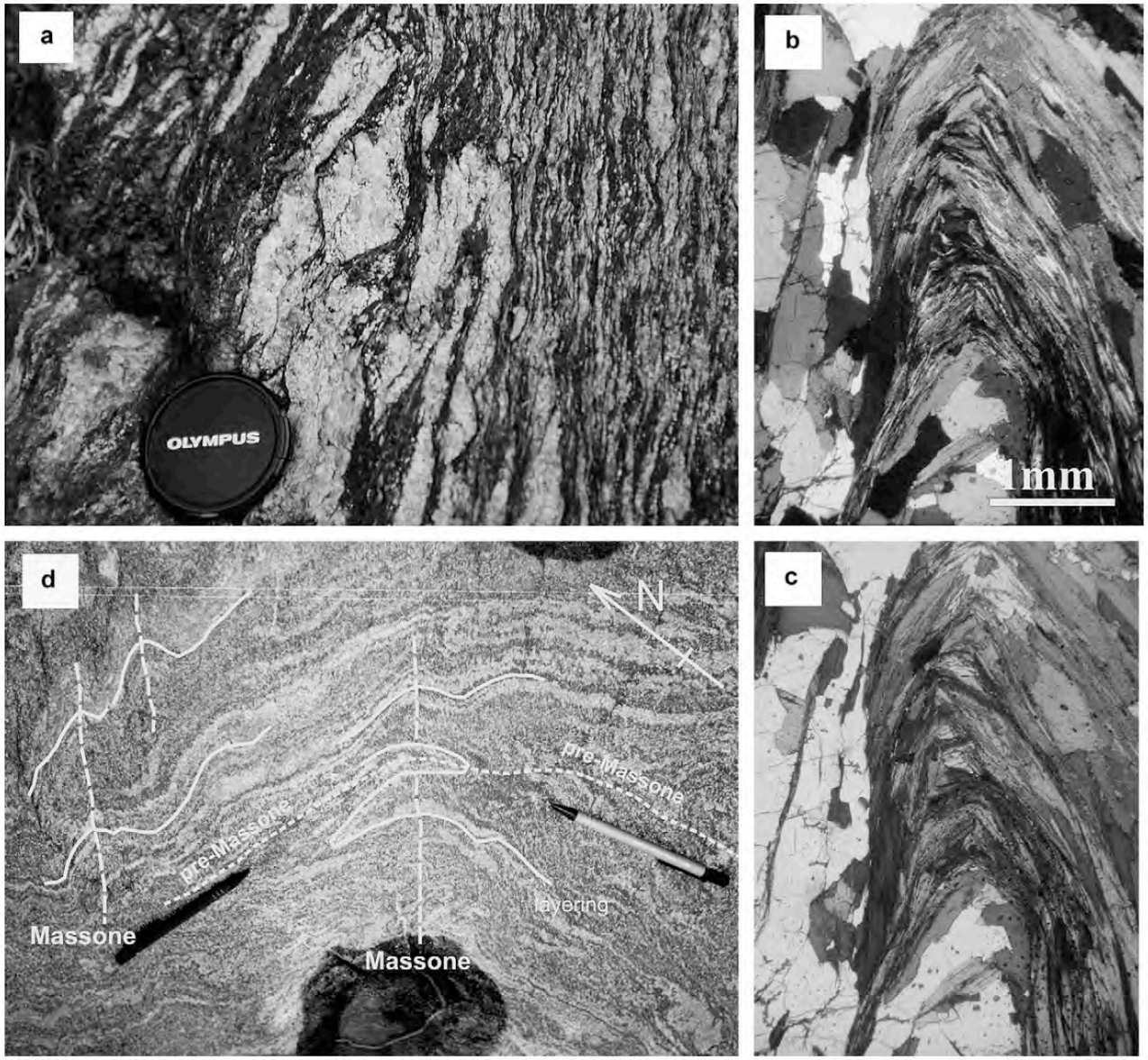

Fig. 7. (a) Intense crenulation cleavage axial planar to the folds of Massone age in migmatitic biotite–sillimanite schist (kinzigite Fm), showing isoclinal folding of leucosome (centre), Loc. Strona river near Strona village. (b and c) Localization of fibrous sillimanite growth into the dilatant hinge of a crenulation of early schistosity in biotite–sillimanite schist of the kinzigite Fm, implying growth of the sillimanite during crenulation. The crenulation cleavage is axial planar to the Massone Antiform. Locality: M. Massone summit (Figs. 2 and 4), crossed-polars (b) and plane-polarized light (c). (d) Vertical view onto small-scale interference of tight pre-Massone minor folds with NE-plunging Massone-age small-scale folds affecting banded amphibolite in the axial region of the Massone Antiform in Val Grande, some 5 km NE of Valle d'Ossola. Axial traces of the two sets of folds are highlighted.

Rutter et al 2009

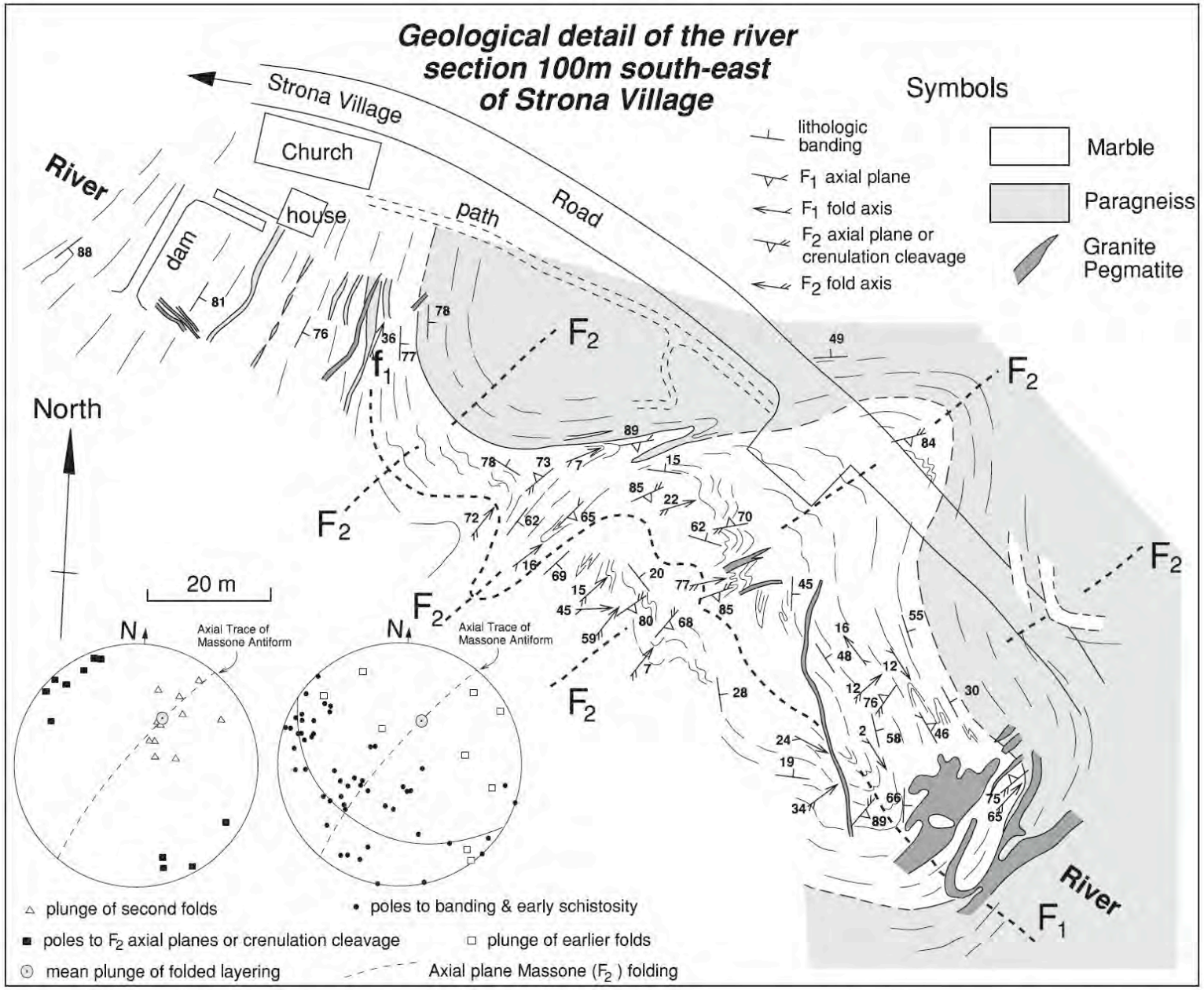

Fig. 8. Detailed map of the F1/F2 fold interference structures displayed in a short section of the Strona river about 100 m south-east of Strona Village (location shown on Fig. 4). Massone folds (F2) plunge moderately to the NW, folding an earlier schistosity and fold axes (F1). Small granite pegmatite bodies crosscut the earlier folds but are folded about axial planes of folds of Massone age.

Rutter et al 2009

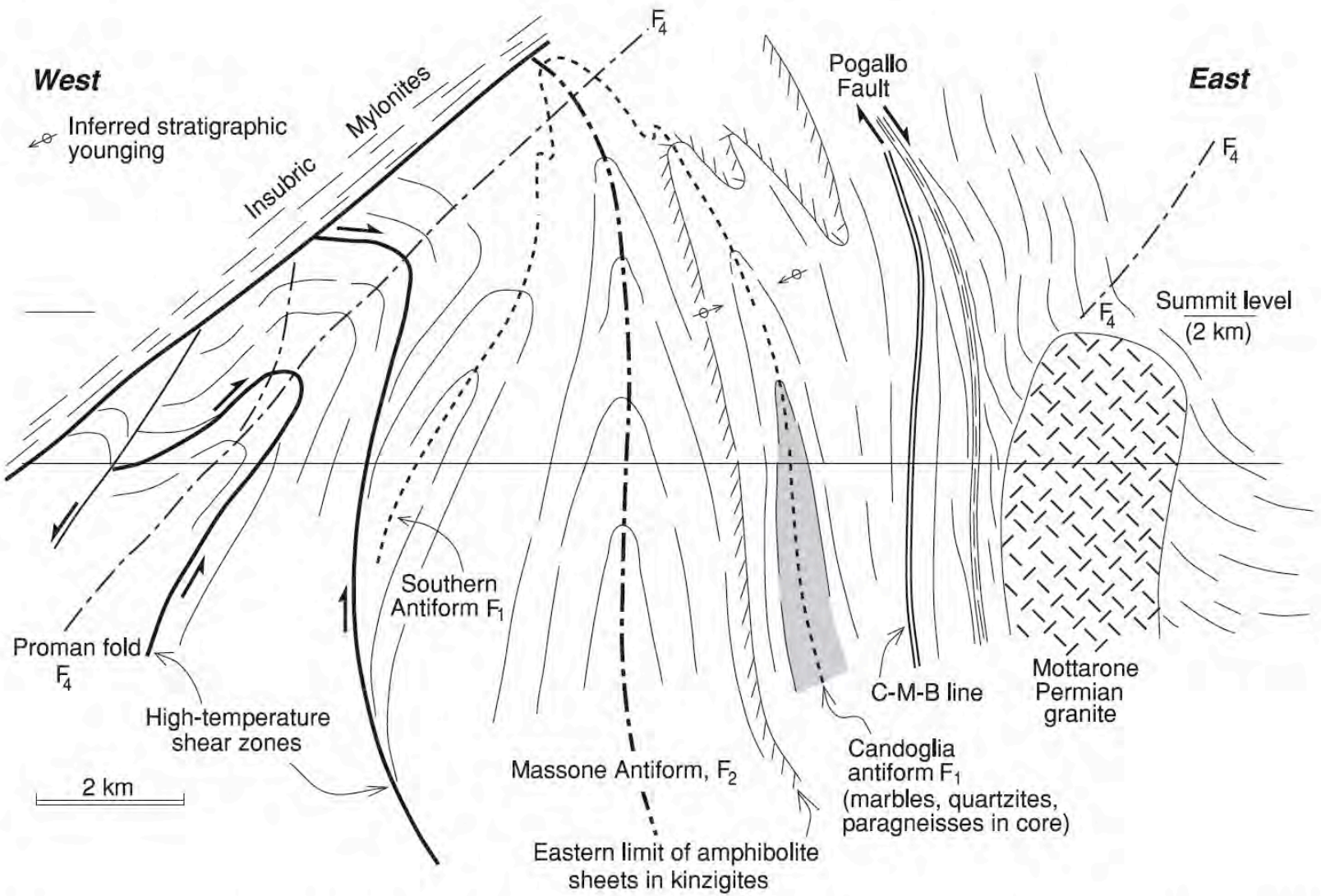

Fig. 9. Outline vertical cross-section parallel to the Valle d'Ossola (location on Fig. 1) to show the relationships between the main structural features. The I-V zone is bounded to the NW by the Insubric mylonite zone, and is in contact with the adjacent S. dei Laghi to the SE across the C-M-B line. Along the contact the S. dei Laghi rocks are near vertical, in common with most of I-V zone rocks, but swing around to a gentle SE dip in the vicinity of the Mottarone granite. The vertical I-V zone rocks are also folded back to the near-horizontal by the Proman fold (axial trace labelled F4), just beneath the Insubric mylonite belt, so that Alpine folding has generated a large monoclinal kink, with the I-V zone comprising most of the steep limb. The earlier, upright Massone Antiform structure also folds the earlier Strona-Candoglia fold core, the latter interpreted to be of equivalent age to the Southern Antiform (Schmid, 1967), which lies on the NW limb of the Massone Antiform.

Rutter et al 2009

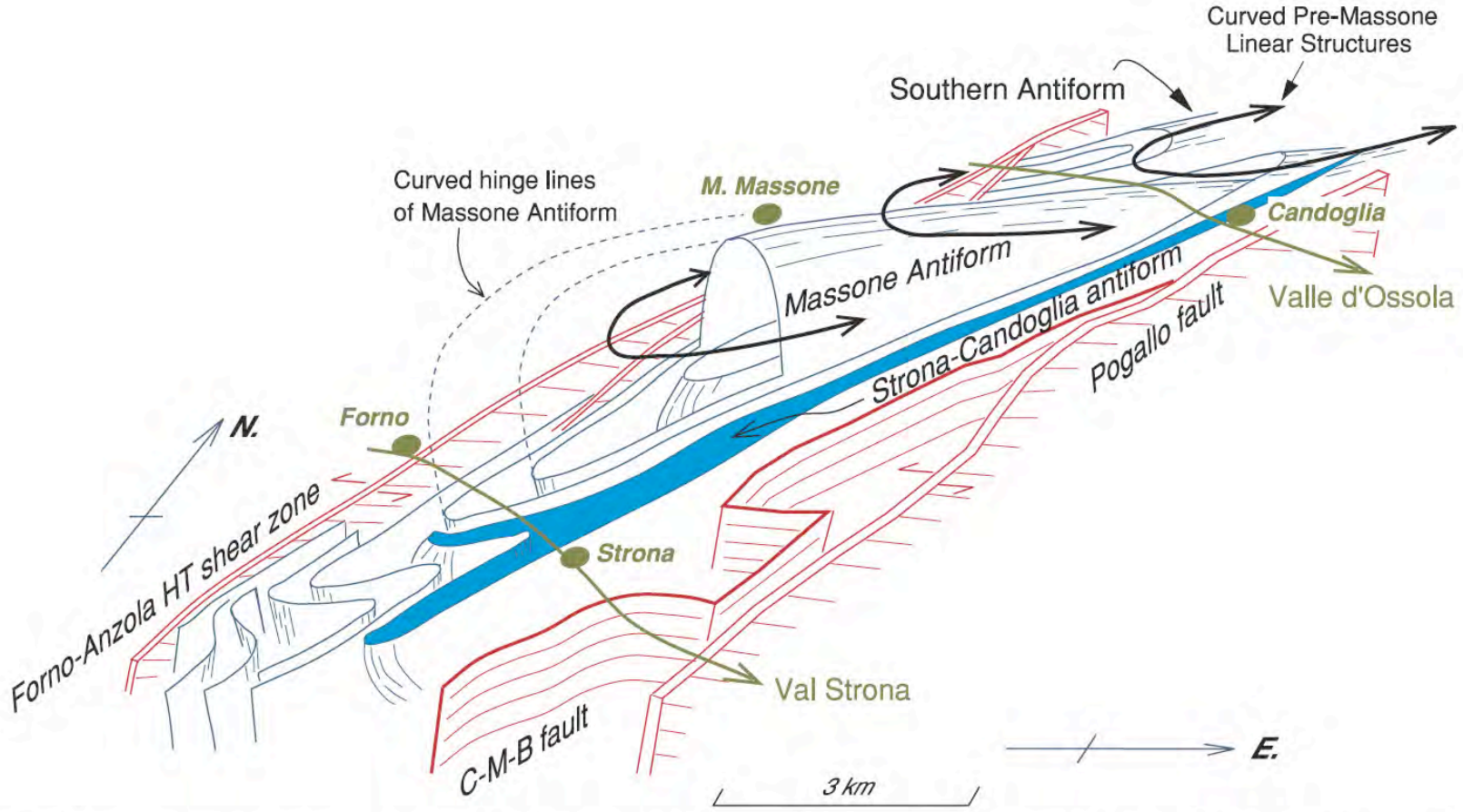

Fig. 10. Block diagram (looking north) to illustrate the three-dimensional geometry of the plunge culmination of the Massone Antiform and the earlier folds (the Southern Antiform and the Strona-Candoglia antiformal syncline), and the major fault surfaces. Pre-Massone mineral lineations and fold axes are curved around the Massone Antiform axial plane to form a type-2 interference geometry.

Rutter et al 2009

Tectonic Environment	Event	Associated Small-Scale Structures	Associated Major Structures
Hercynian Orogeny or earlier.	Pre-Massone folding (F_1).	Mineral stretching lineation, axial planar schistosity. Early folds, migmatization and regional metamorphism.	Strona-Candoglia syncline. Southern Antiform.
	Massone folding (F_2).	Axial-planar crenulation fabric. Folding of leucosomes and granitoid sheets.	Massone Antiform.
	Post-Massone folding (F_3).	Open, chevron-style coarse crenulation. Axial-planar crenulation fabric.	No obvious large-scale structures.
Post-orogenic extension. (Permo-Triassic)	Intrusion of Mafic Formation. Ductile stretching.	Contact metamorphism and migmatization.	Mafic Formation. C-M-B line shearing and igneous activity.
	Regional subsolidus stretching.	Linear features aligned where strain is highest. High temperature shear zones.	High-temperature shear zone formation. Pogallo faulting.
Alpine Orogenesis.	Alpine backthrusting on Insubric Line and associated folding (F_4) and faulting.	Brittle faults bearing greenschist assemblages. Some with frictional melting. Increasing frequency towards Insubric line.	Regional-scale monoclinal structure forms - Proman fold and folding about Serie dei Laghi granites.

1. Summary (time sequence top to bottom) of the tectonic events and associated small and large-scale structures produced in the Ivrea-Verbano zone.

Rutter et al 2009

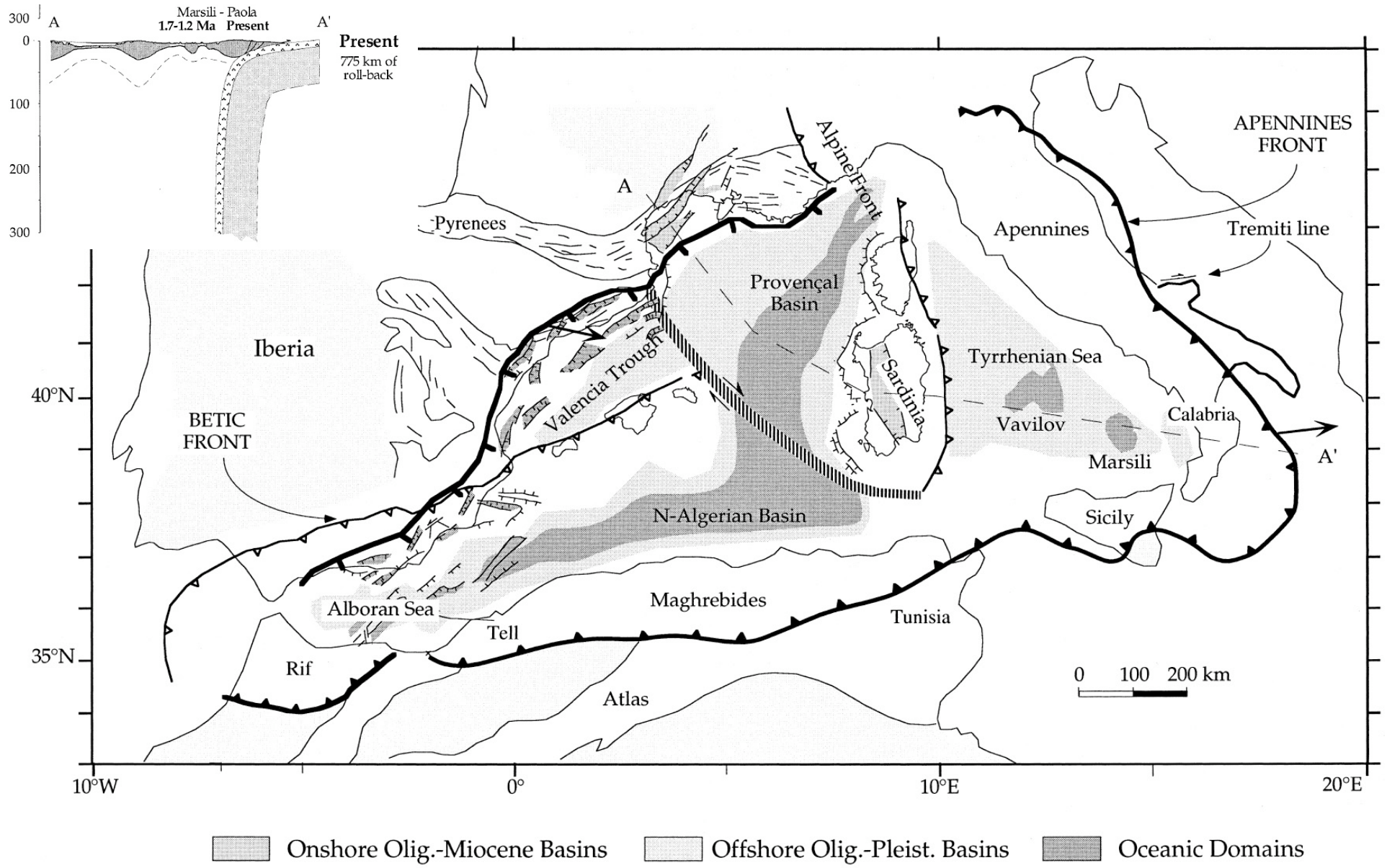

Fig. 5. The western Mediterranean is composed of sub-basins becoming younger from west to east. They developed in the hangingwall of the 'eastward' retreating Apenninic subduction, as back-arc basins, during the last 30 Ma. These sub-basins are triangular in shape. *A–A′* shows location of the section shown in Fig. 1.

Present Tectonic Map

Gueguen et al 1997

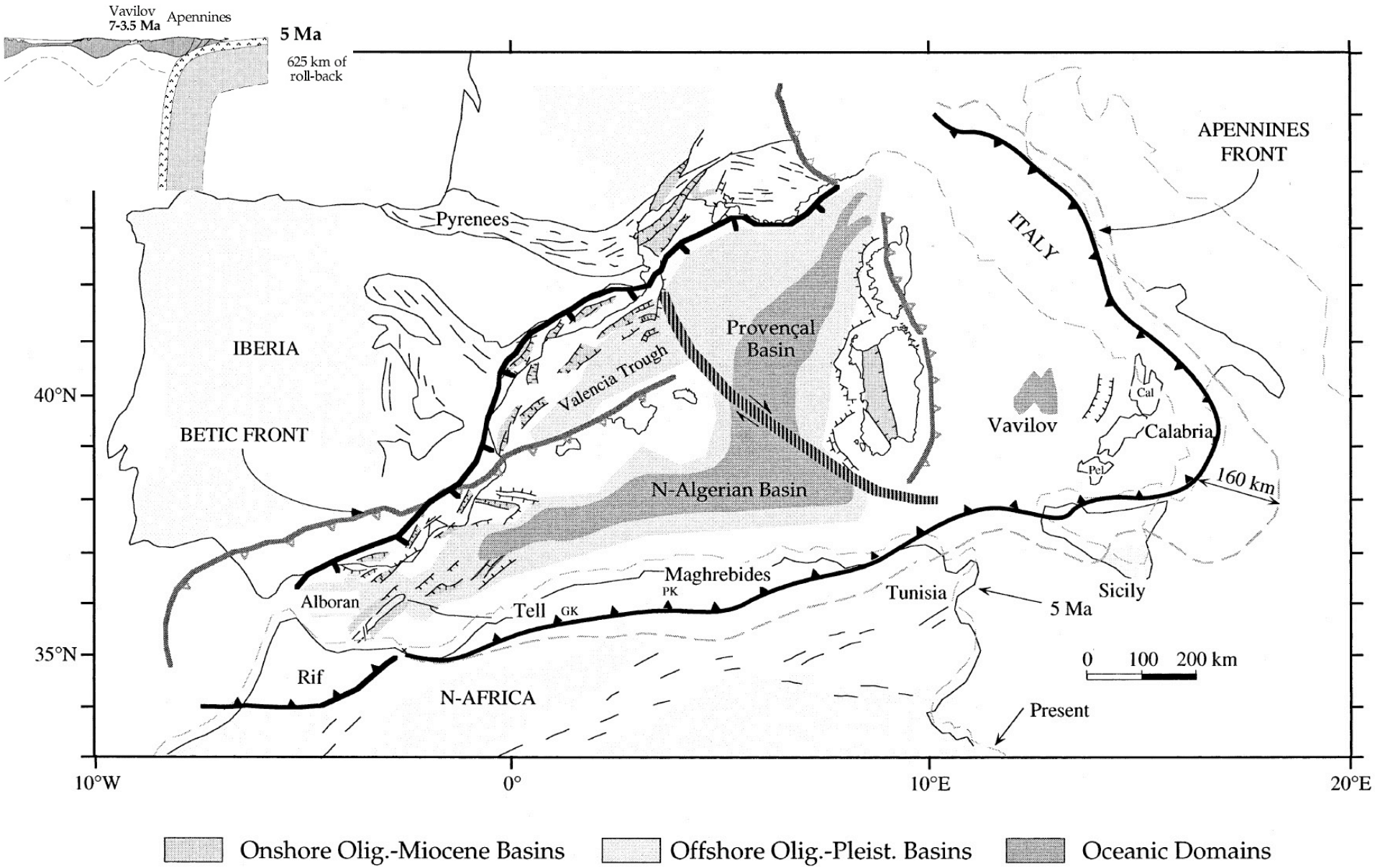

Fig. 4. Early Pliocene palaeotectonic reconstruction. The Tyrrhenian basin began to develop oceanic crust in the Vavilov area. The entire system associated with the Apenninic subduction migrated eastward at rates up to 50 mm/year.

5 Ma Paleotectonic Map

Gueguen et al 1997

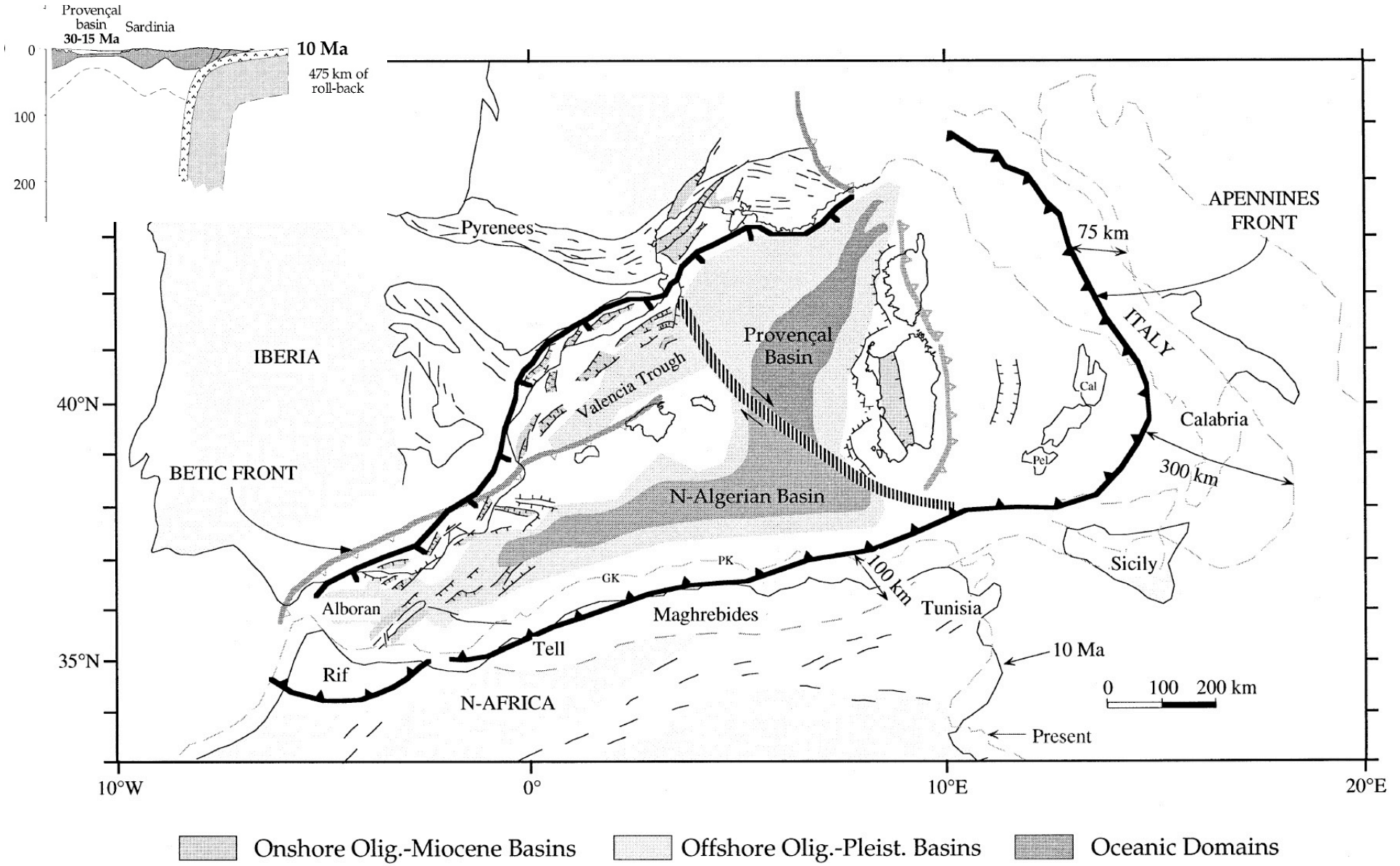

Fig. 3. Most of the western Mediterranean basins had already opened during Tortonian times. Both the trench of the Apennine subduction and related focus of back-arc

10 Ma Paleotectonic Map

Gueguen et al 1997

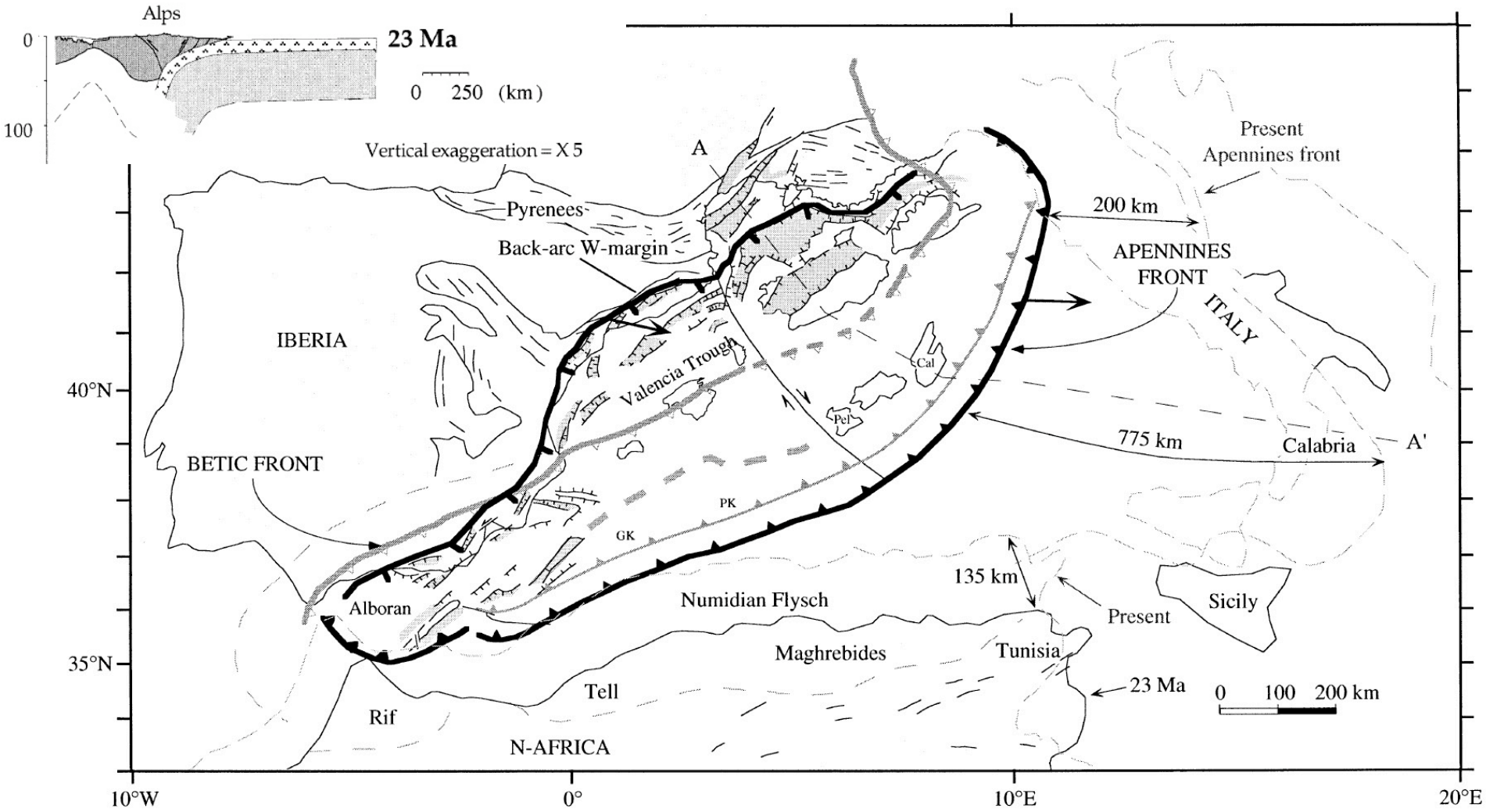

Fig. 2. Early Miocene palaeotectonic reconstruction of the western Mediterranean showing the extensional system (Provençal–Valencia–Alboran), considered as the back-arc basin of the west-directed Apenninic subduction (in black). Note the eastward vergence of both the Apenninic trench and of the back-arc extension. In grey are marked the fronts of the Alpine–Betic orogen which is cross-cut by the zone of back-arc extension. The back-arc basin of the Apenninic subduction fragmented the Alpine–Betic orogen into the segmented basins. Note the distance between the reconstructed Early Miocene arc and its present position (775 km) with respect to the contemporaneous, but smaller north-northwestward motion of Africa relative to Europe (135 km). *A–A′* shows location of the section shown in Fig. 1.

23 Ma Paleotectonic Map

Gueguen et al 1997

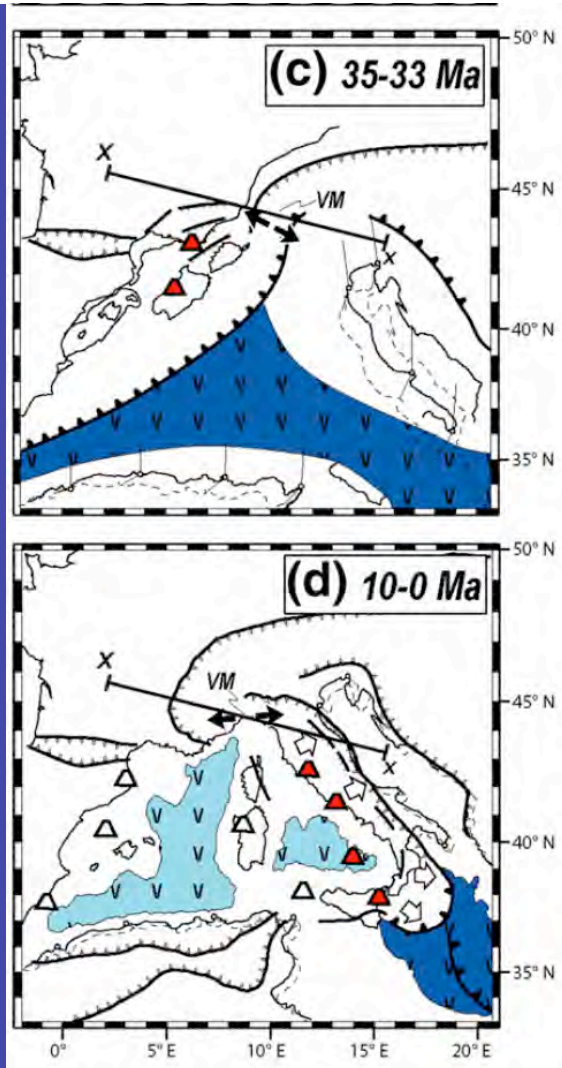

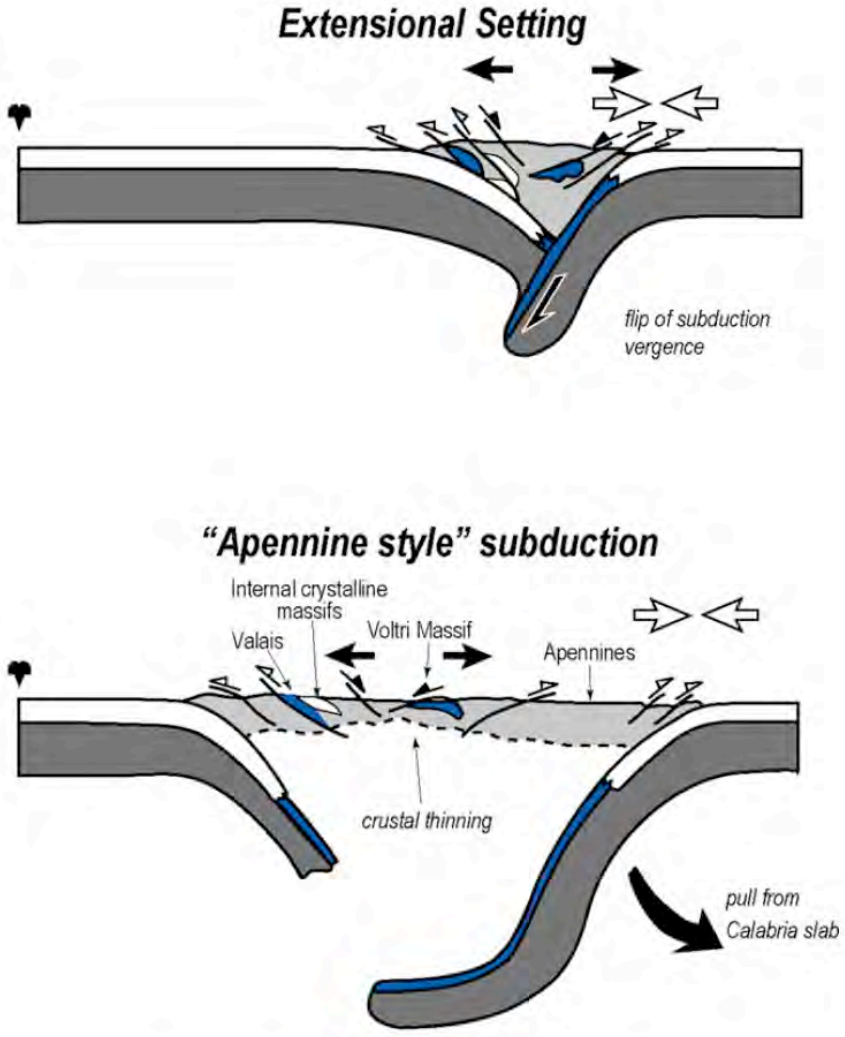

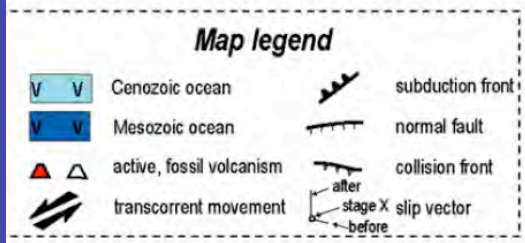

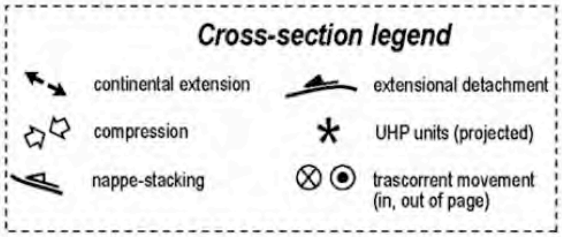

Western Alpine-Apennine Tectonic History 35-0 Ma

Vignarolli et al 2008

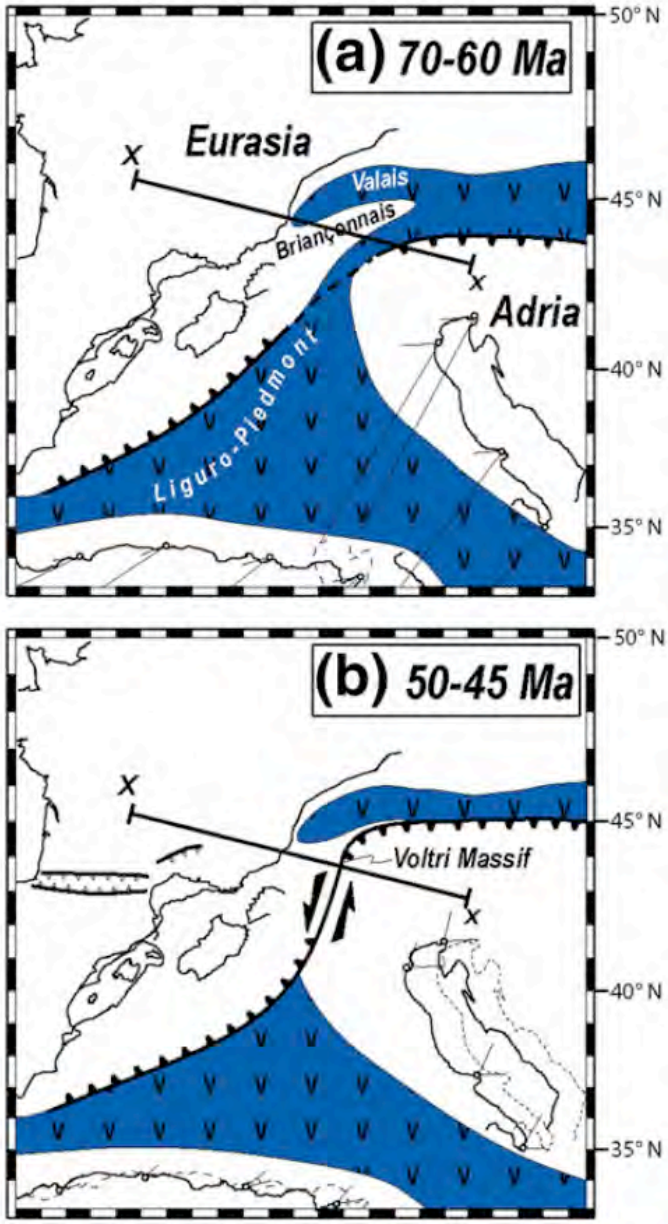

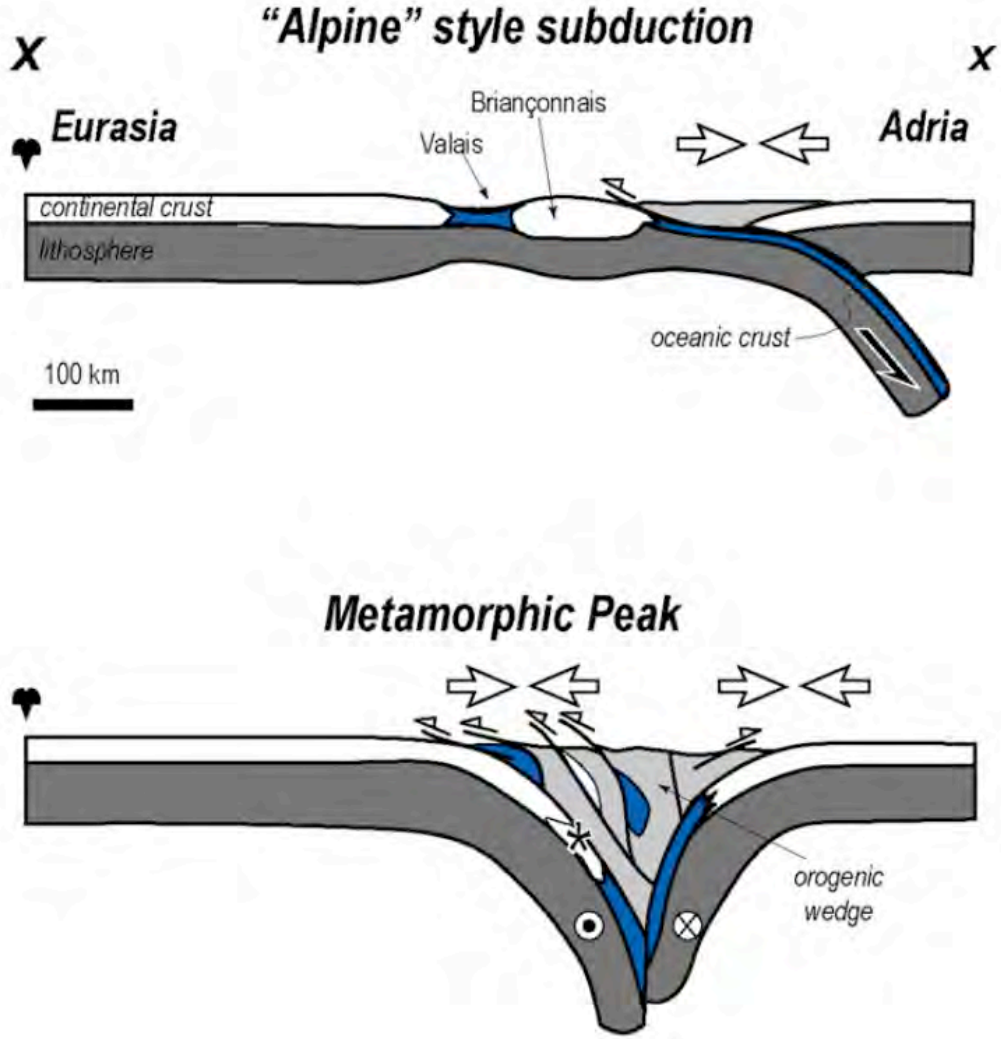

Western Alpine Tectonic History 70-45 Ma

Vignarolli et al 2008

Western Alpine-Apennine Tectonic History 70-0 Ma

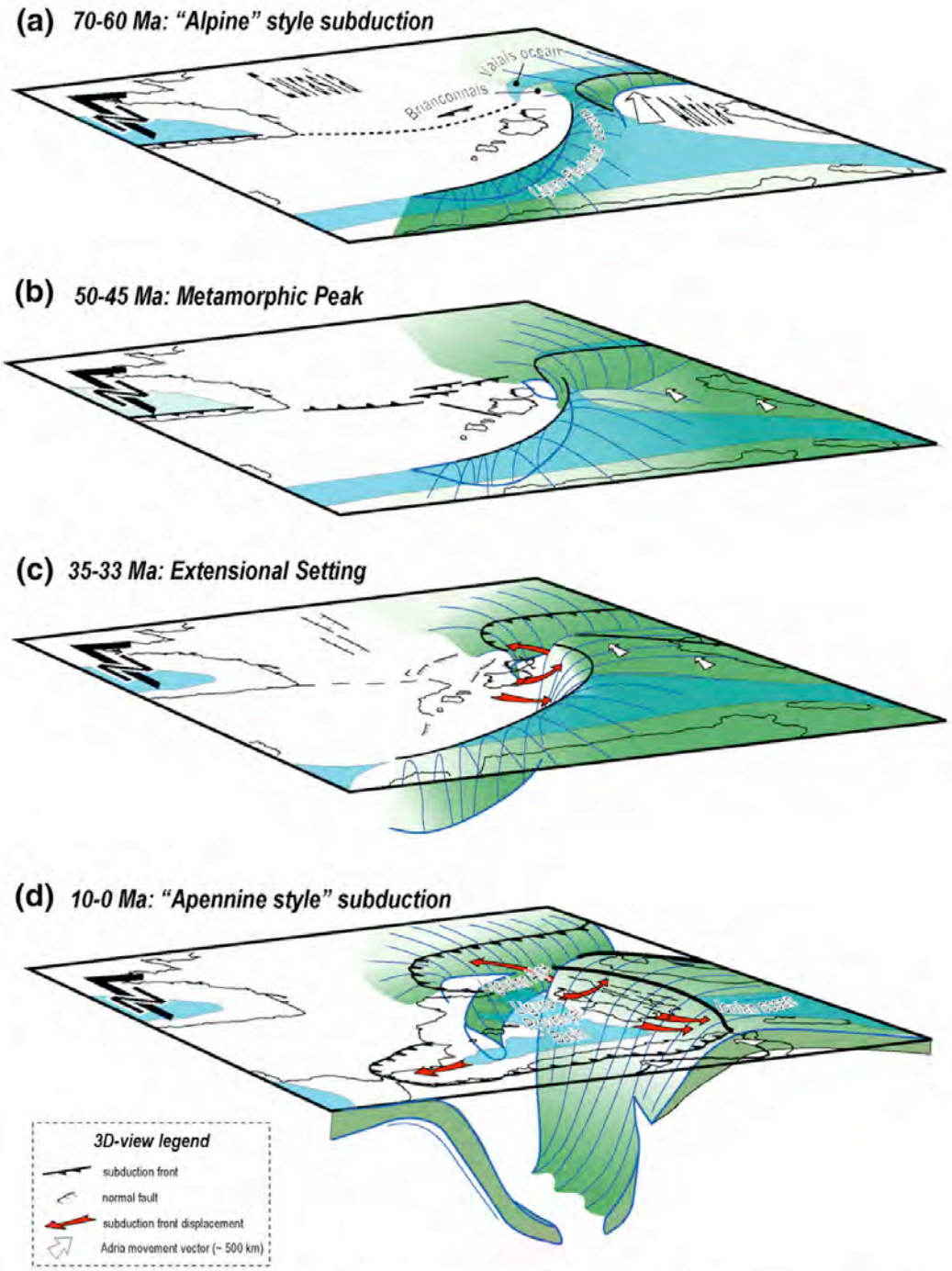

Vignarolli et al 2008

chematic 3D-view of the kinematic reconstruction of the Alps–Apennines belt system, showing as the two orogenic segments progressively separated and

Western Mediterranean Tectonic history ~23-10 Ma

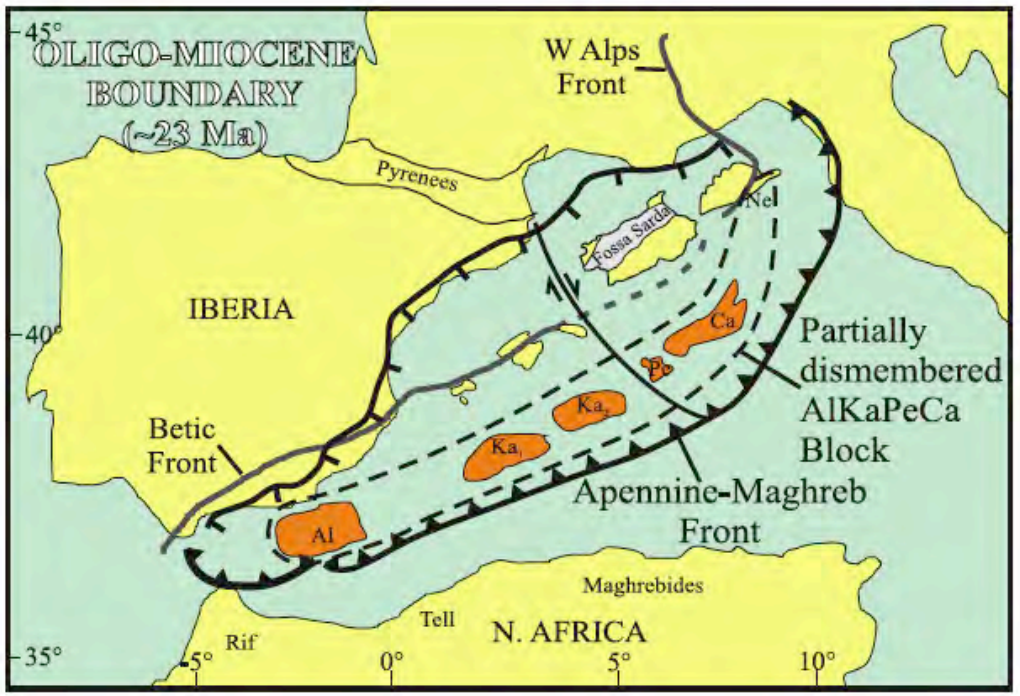

Lustrino et al 2009

Four Models Western Mediterranean Paleocene ~65 Ma

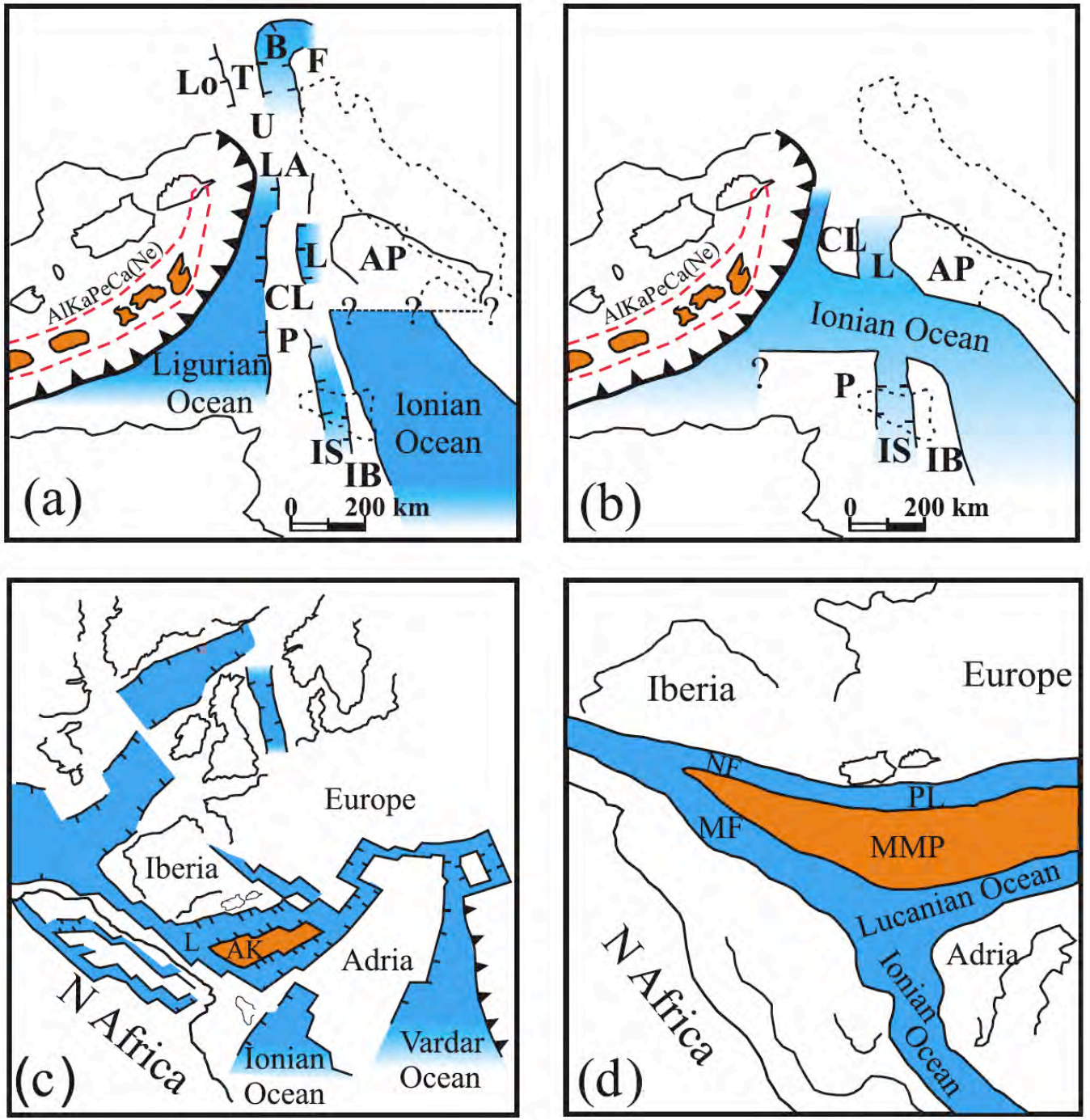

Figure 8

Lustrino et al 2009

65-0 My Tethys Plate History

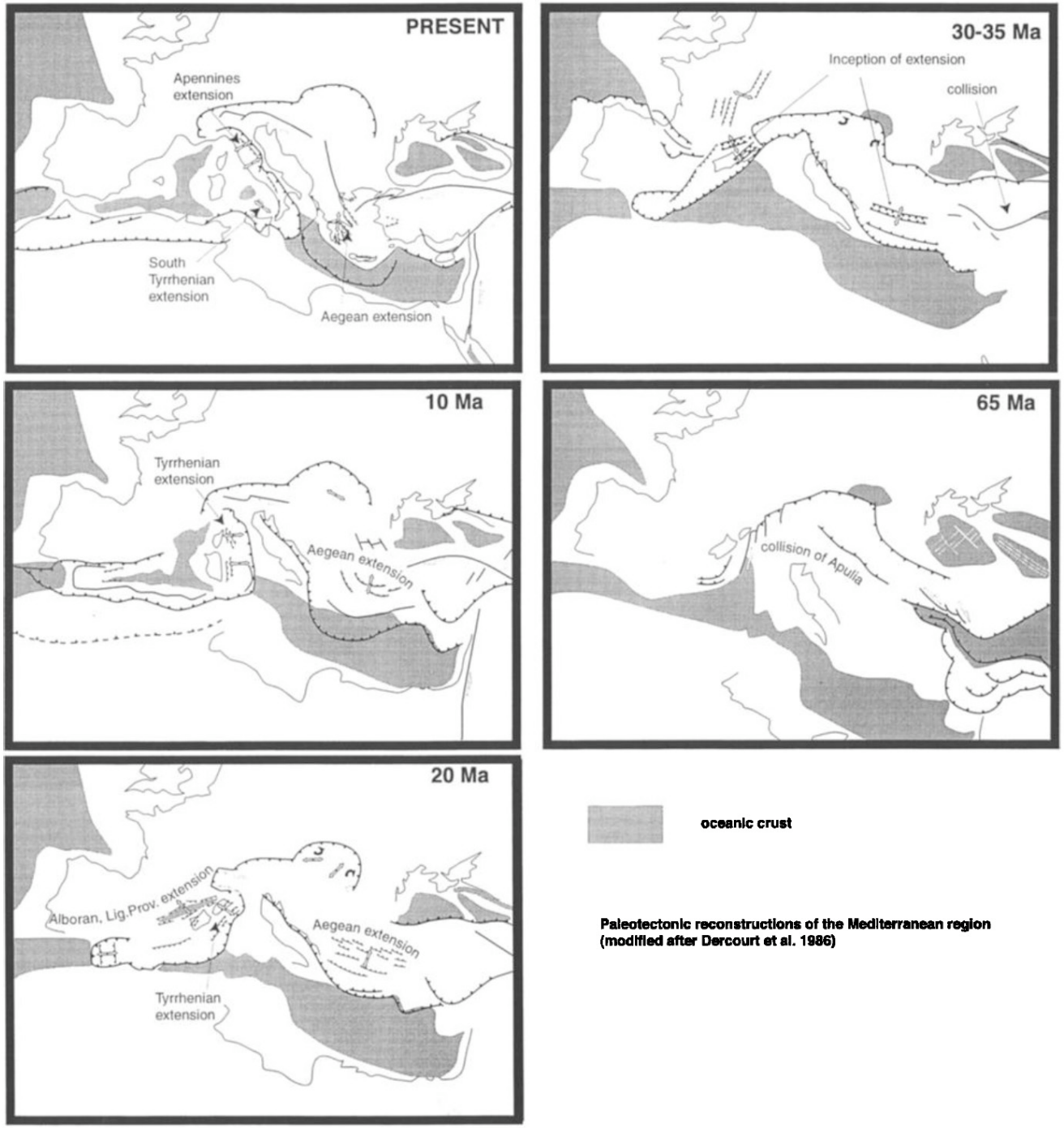

Paleotectonic reconstructions of the Mediterranean region (modified after Dercourt et al. 1986)

Jolivet & Faccenna 2000

Western Tethys Mesozoic Plate Model

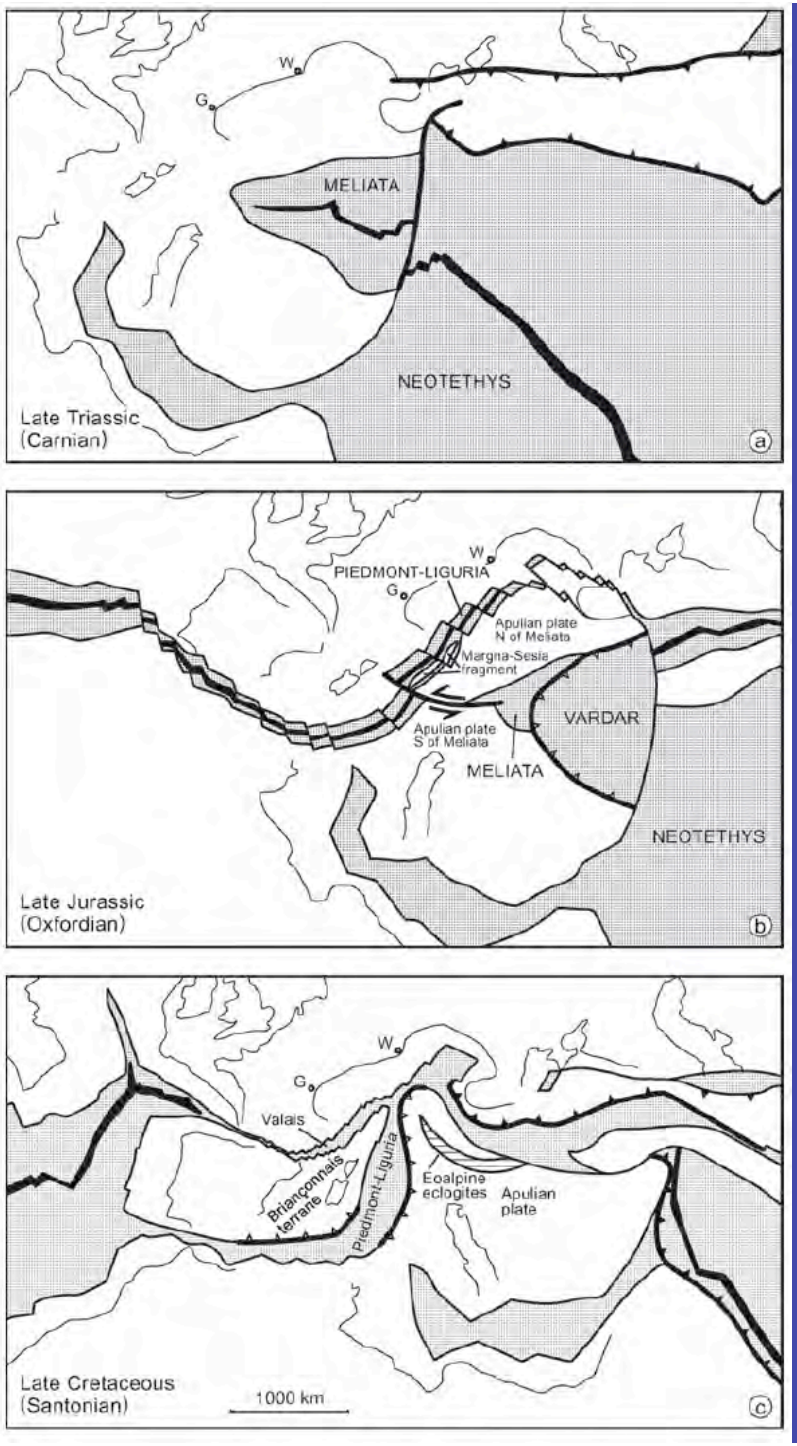

Schmidt et al 2004

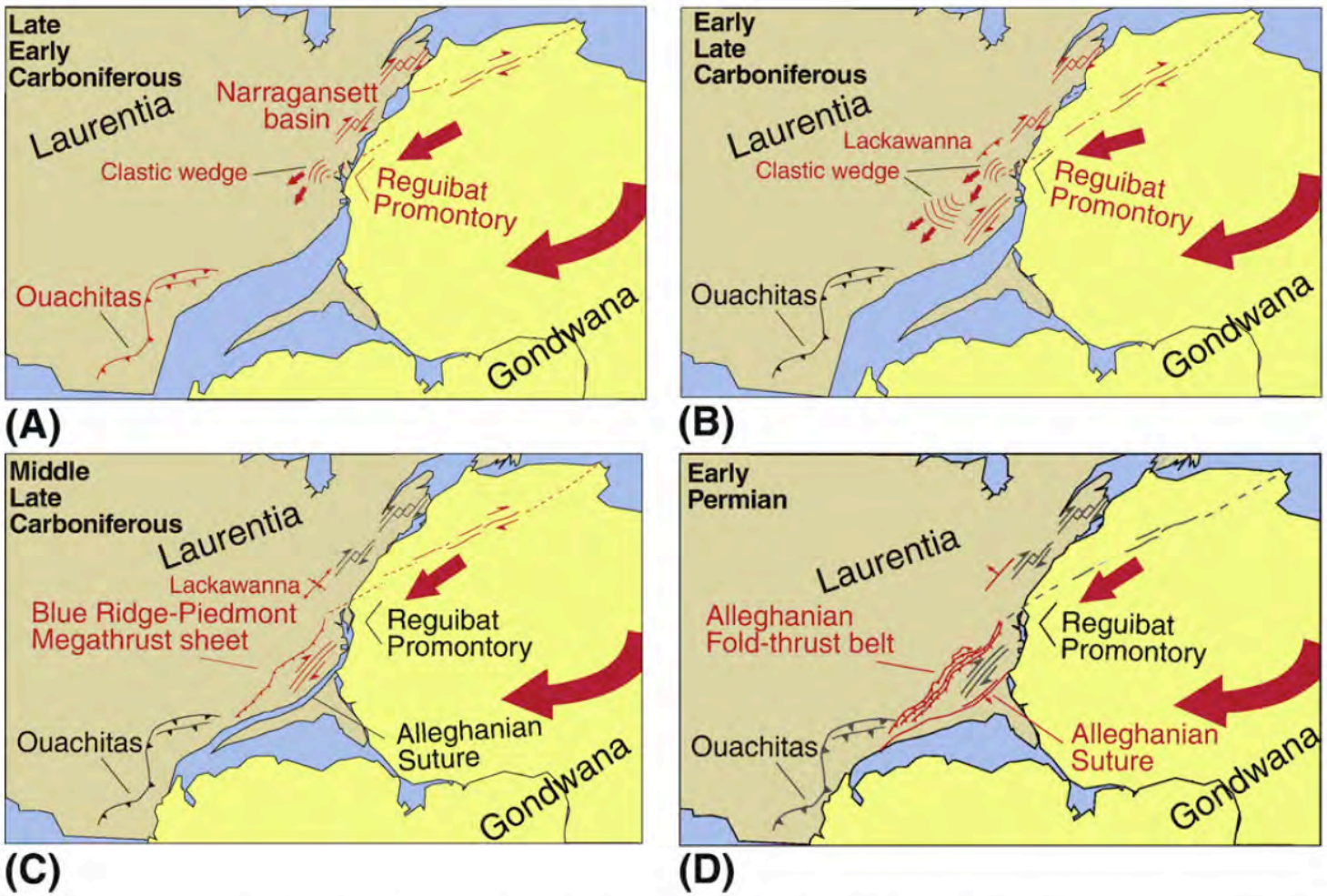

. 15. Oblique rotational collision between Laurentia and Gondwana according to Hatcher (2002). Symbols in red identify features active during time interval represented. Initial contact between Laurentia and Gondwana during Late Mississippian, (B) southward motion and clockwise rotation of Gondwana during Early Pennsylvanian, continued rotation and southward movement of Gondwana in Late Pennsylvanian, and (D) head-on Laurentia–Gondwana collision in Early Permian.

Nance et al 2010

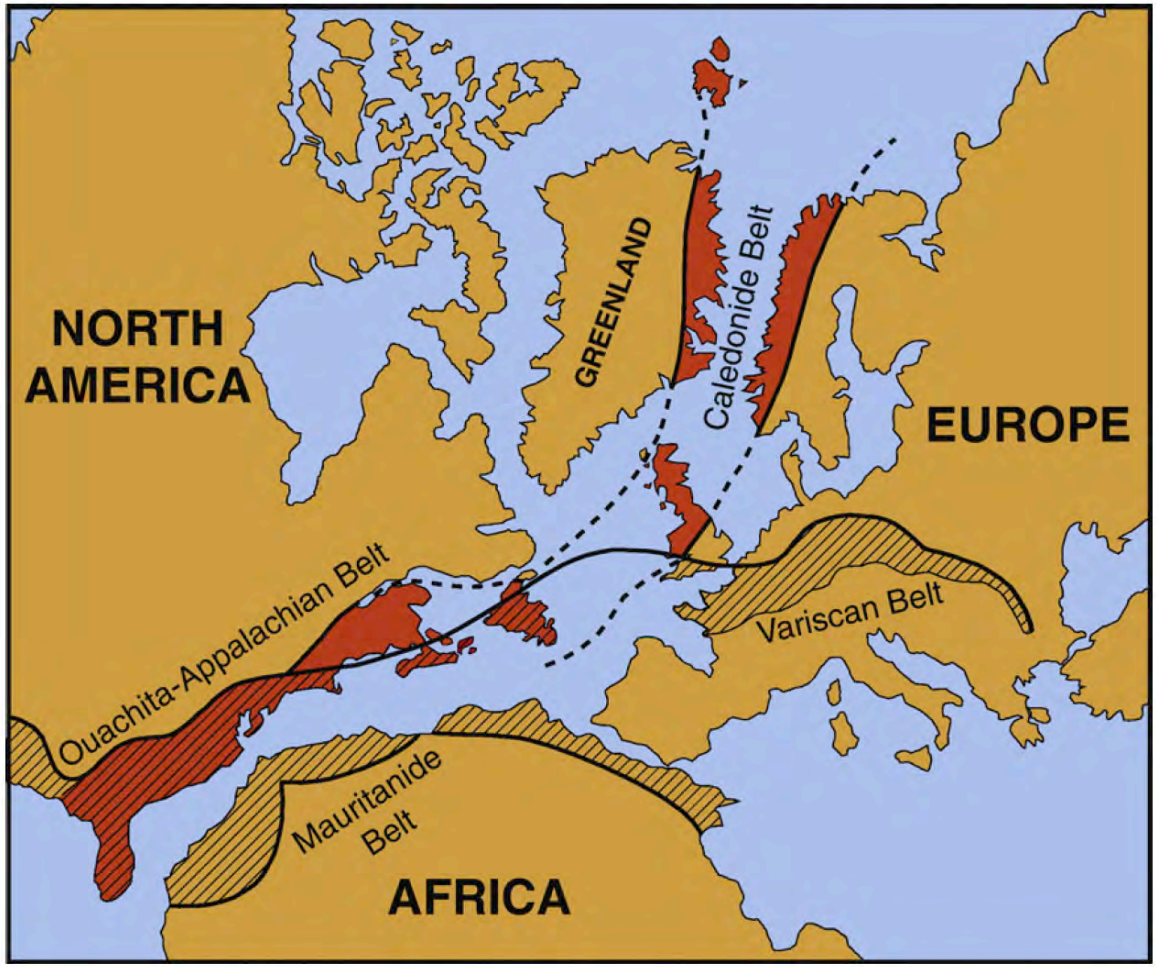

Fig. 2. Continuity of the Ouachita–Appalachian belt of North America with the Caledonian and Variscan belts of Europe and the reactivated Mauritanide belt of West Africa in a Pangaea fit of the North Atlantic. Cross hatching identifies areas of Late Palaeozoic (Variscan–Alleghanian–Ouachita) deformation associated with closure of the Rheic Ocean.

Nance et al 2010

Nance
et al 2010

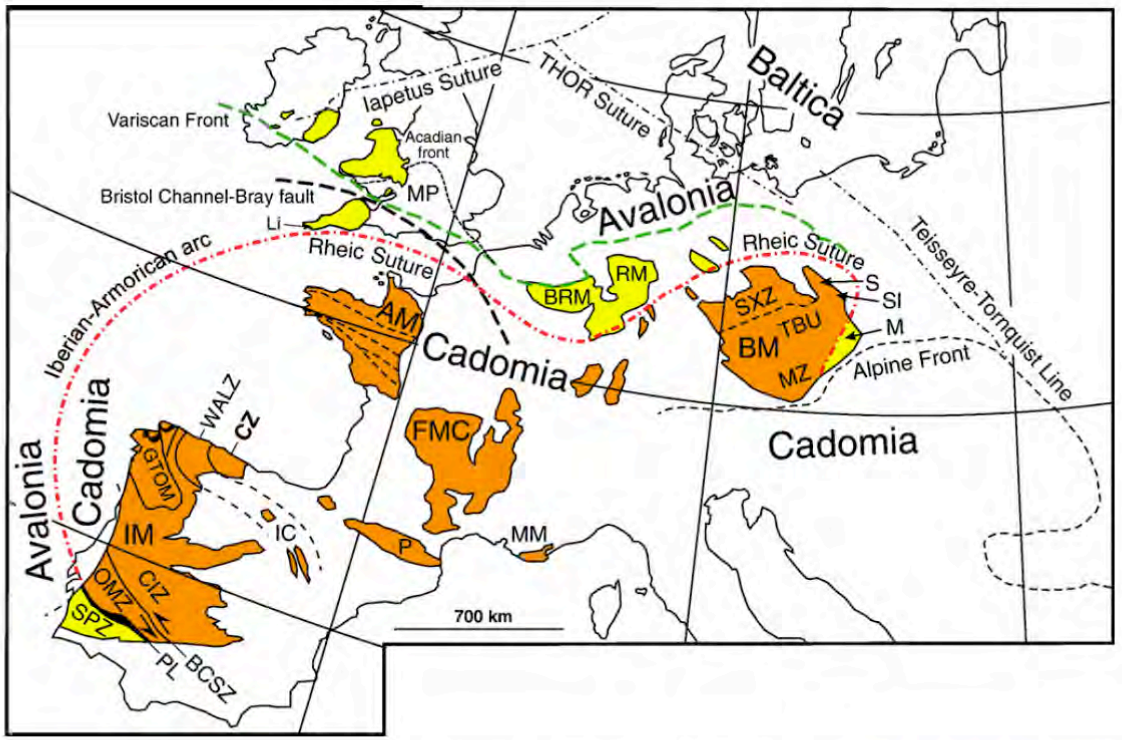

Fig. 5. Location of the Rheic suture with respect to Cadomian and Variscan Massifs in southeastern and central Europe (after Linnemann et al., 2007). Abbreviations: (1) Iberia—BCSZ = Badajoz-Cordoba Shear zone, CIZ = Central Iberian zone, CZ = Cantabrian zone, IC = Iberian Chains, IM = Iberian Massif, GTOM = Galicia Trás-os-Montes zone, MM = Maures Massif, OMZ = Ossa-Morena zone, P = Pyrénées, PL = Pulo de Lobo oceanic units, SPZ = South Portuguese zone, WALZ = West Asturian Leonese zone, (2) Western Europe—AM = Armorican Massif, FMC = French Massif Central, Li = Lizard Ophiolite, (3) Central and Eastern Europe—BM = Bohemian Massif, BRM = Brabant Massif, M = Moravo-Silesian zone, MP = Midland Platform, MZ = Moldanubian zone, RM = Rhenish Massif, S = Sudetes, SI = Sleza ophiolite, SXZ = Saxo-Thuringian zone, TBU = Teplá-Barrandian Unit. Black = oceanic rocks of the Pulo de Lobo suture (Beja-Acebuches ophiolite) in southern Iberia and ophiolitic units of allochthonous complexes in NW Spain (Galicia).

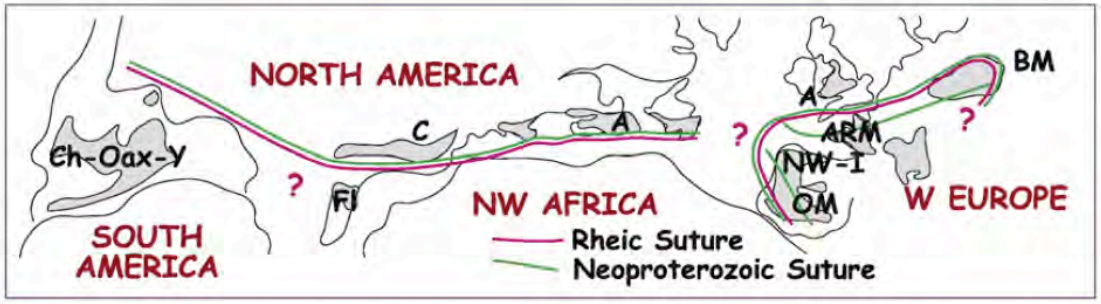

Fig. 3. Location of Rheic suture on Early Mesozoic reconstruction of the North Atlantic and its close correspondence with sutures associated with the accretion of arc terranes to the northern Gondwanan margin in the Late Neoproterozoic (from Murphy et al., 2006a). Abbreviations: A = Avalonia, Arm = Armorica, BM = Bohemian Massif, C = Carolinia, CAD = Cadomia, Ch = Chortis, Fl = Florida, NW-I = northwest Iberia, Oax = Oaxaquia, OM = Ossa Morena, Y = Yucatan.

Fig. 1. Early Silurian reconstruction of the Rheic Ocean immediately prior to the closure of Iapetus by way of subduction beneath Laurentia (toothed red line). Stippled areas denote inferred regions of thinned and/or anomalous thickness of continental and arc crust (simplified after Pickering and Smith, 1995, with Cadomia placed adjacent to Gondwana). Rheic ridge-transform system purely schematic. Heavy black lines trace Tornquist suture zone.

Nance et al 2010

The Assembly of Pangea 340 to 300 Ma

Stampfli & Borel 2002

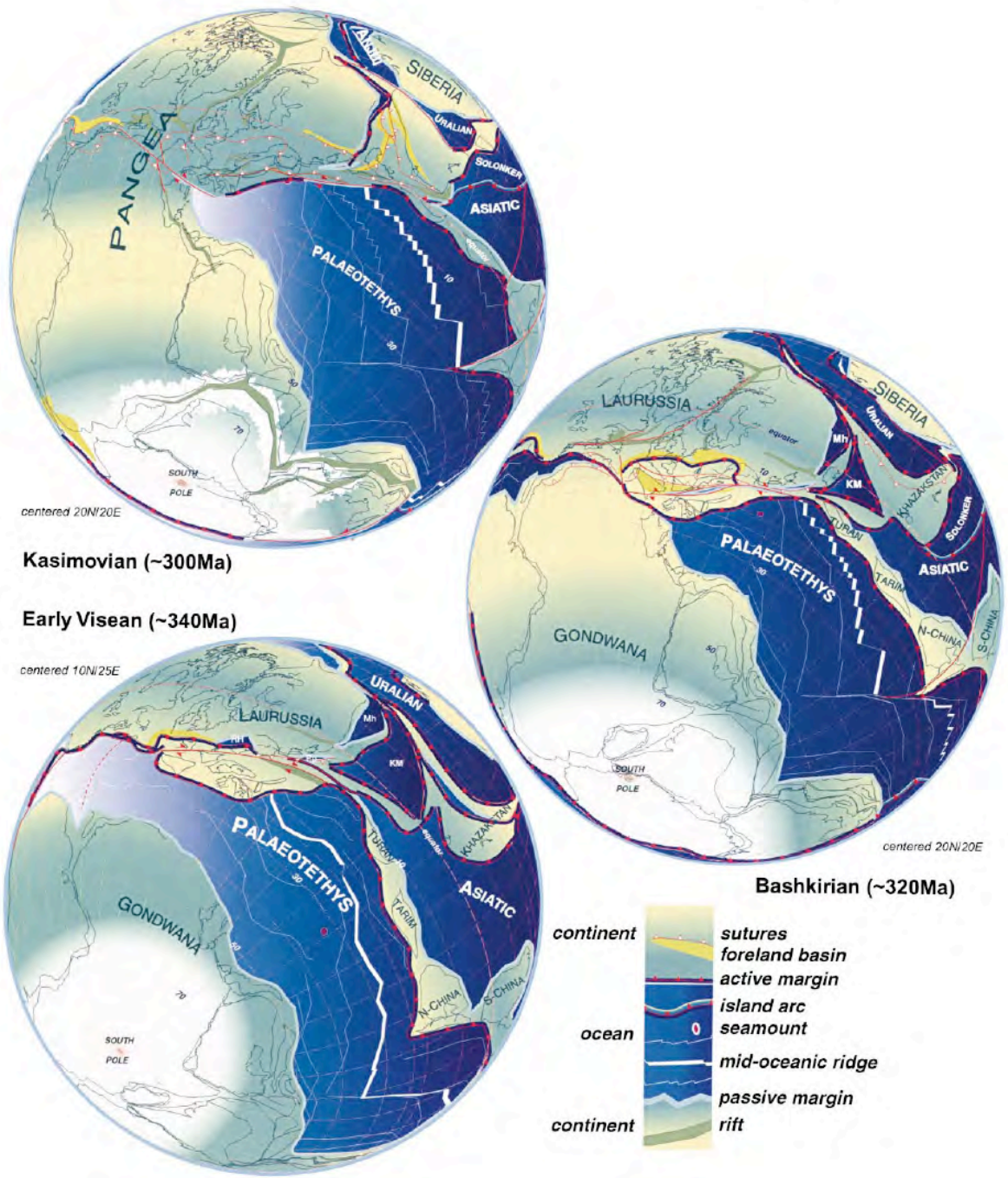

Opening of the Tethys Oceans 290-250Ma

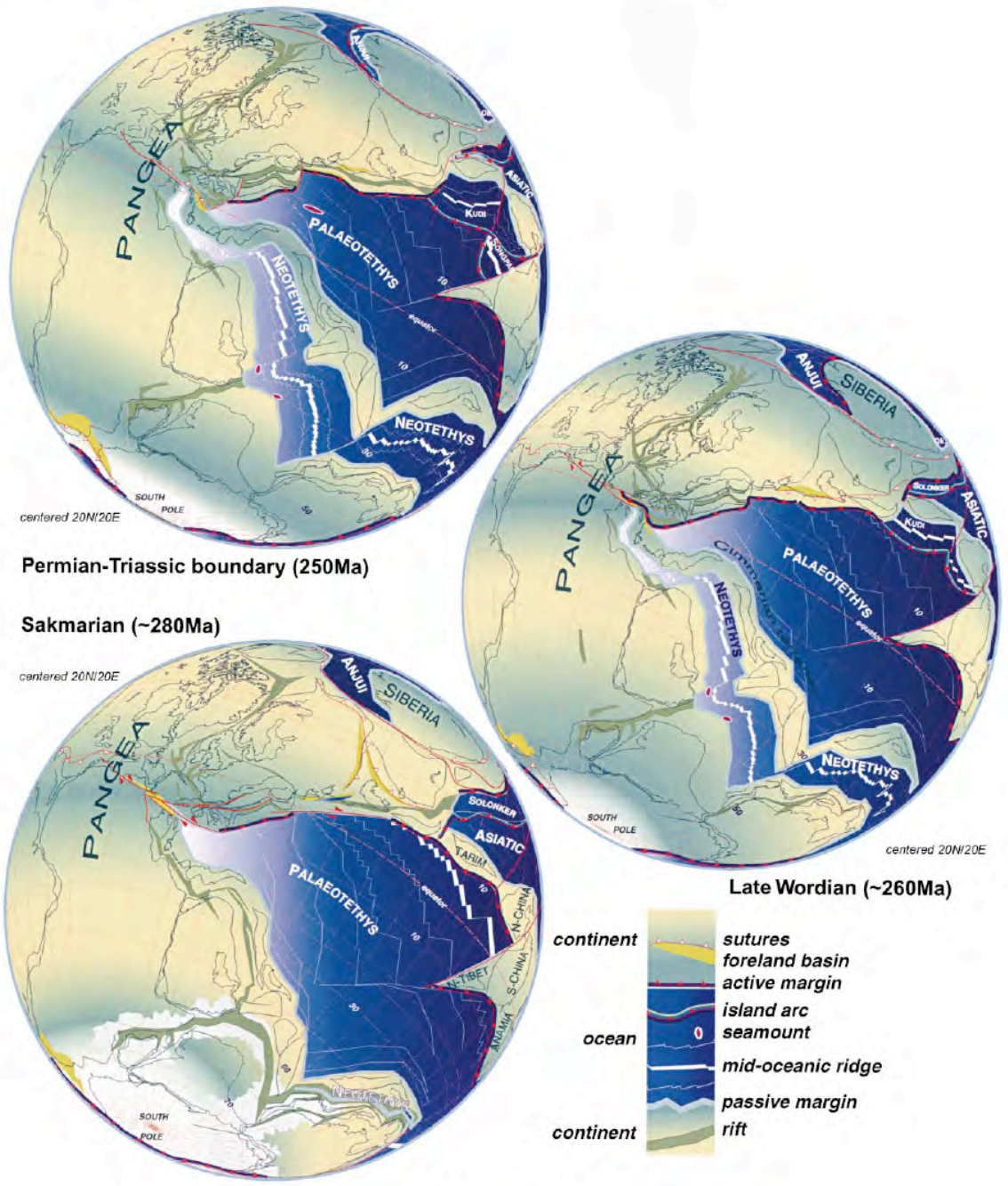

Fig. 6. See legend of Fig. 3.

Stampfli & Borel 2002

Sea floor spreading In the Alpine Tethys And Vardar Seas 140-85 Ma

Stampfli & Borel 2002

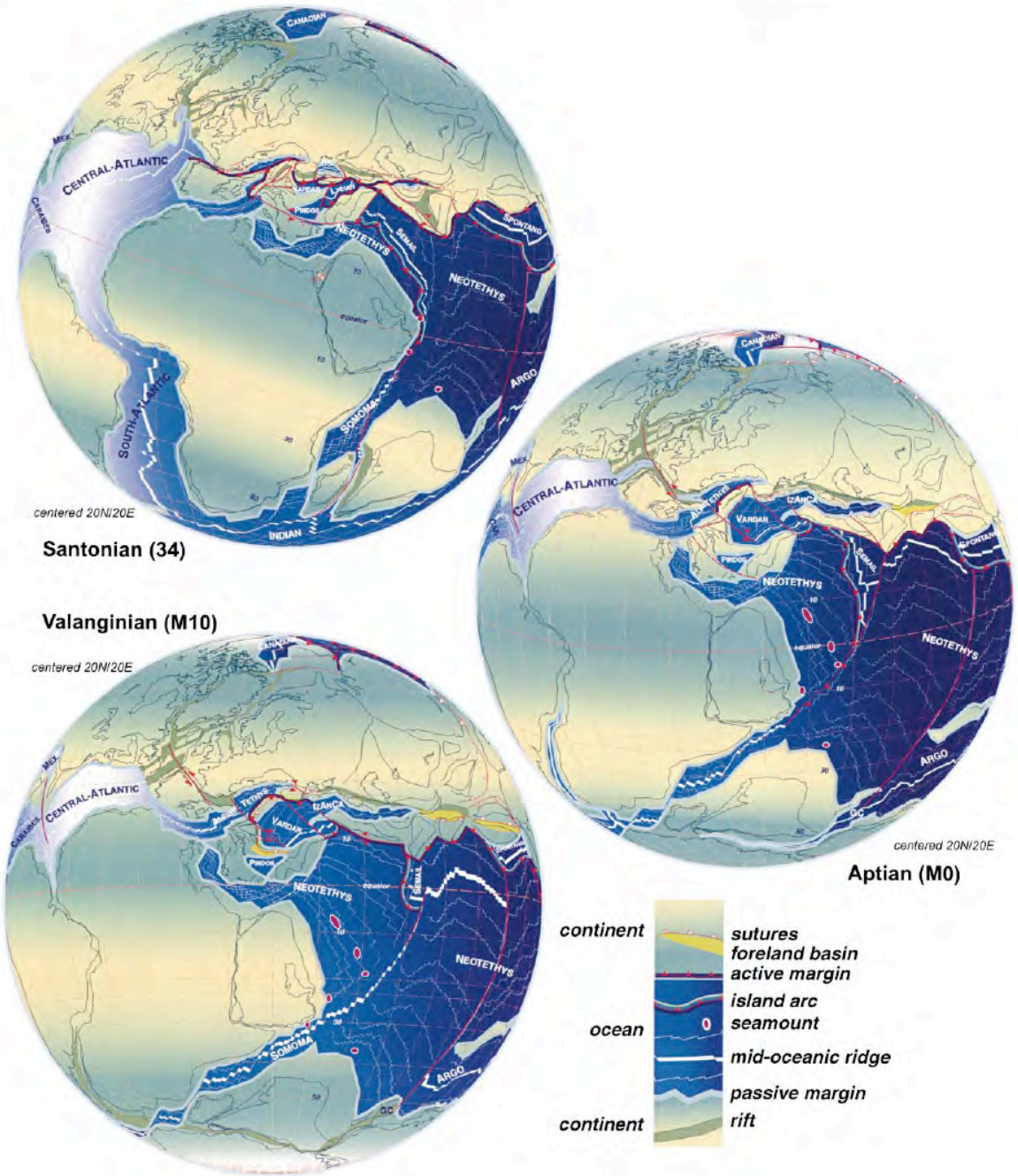

Fig. 9. See legend of Fig. 3.

80 Ma Alpine Tethys Sea Floor Spreading